# EXPERIMENTAL AND NUMERICAL INVESTIGATION OF THE FRETTING FATIGUE OF DISSIMILAR MATING SURFACES

A THESIS SUBMITTED TO
THE GRADUATE SCHOOL OF NATURAL AND APPLIED SCIENCES
OF
MIDDLE EAST TECHNICAL UNIVERSITY

BY

YEZDAN MEDET KORKMAZ

IN PARTIAL FULFILLMENT OF THE REQUIREMENTS
FOR
THE DEGREE OF MASTER OF SCIENCE
IN
AEROSPACE ENGINEERING

SEPTEMBER 2019

Approval of the thesis:

**EXPERIMENTAL AND NUMERICAL INVESTIGATION OF THE FRETTING FATIGUE OF DISSIMILAR MATING SURFACES**

submitted by **YEZDAN MEDET KORKMAZ** in partial fulfillment of the requirements for the degree of **Master of Science in Aerospace Engineering Department, Middle East Technical University** by,

Prof. Dr. Halil Kalıpçılar
Dean, Graduate School of **Natural and Applied Sciences** _____

Prof. Dr. İsmail Hakkı Tuncer
Head of Department, **Aerospace Engineering** _____

Assoc. Prof. Dr. Demirkan Çöker
Supervisor, **Aerospace Engineering, METU** _____

**Examining Committee Members:**

Prof. Dr. Altan Kayran
Aerospace Engineering, METU _____

Assoc. Prof. Dr. Demirkan Çöker
Aerospace Engineering, METU _____

Assoc. Prof. Dr. Ercan Gürses
Aerospace Engineering, METU _____

Assoc. Prof. Dr. Yıldırım Kemal Yıllıkçı
Faculty of Aerospace Sciences, AYBU _____

Assoc. Prof. Dr. İlker Temizer
Mechanical Engineering, Bilkent Uni. _____

Date: 11.09.2019

**I hereby declare that all information in this document has been obtained and presented in accordance with academic rules and ethical conduct. I also declare that, as required by these rules and conduct, I have fully cited and referenced all material and results that are not original to this work.**

Name, Surname: Yezdan Medet Korkmaz

Signature:

# ABSTRACT

## EXPERIMENTAL AND NUMERICAL INVESTIGATION OF THE FRETTING FATIGUE OF DISSIMILAR MATING SURFACES

Korkmaz, Yezdan Medet
Master of Science, Aerospace Engineering
Supervisor: Assoc. Prof. Dr. Demirkan Çöker

September 2019, 93 pages

Fretting fatigue experiments and simulations were performed for dissimilar mating materials. In the first part of the study, experiments were conducted using different pad materials to clarify the effect of fretting fatigue on the dissimilar mating materials in terms of friction force, contact surfaces, and fatigue life of the substrate material. Steel and Aluminum pad materials were used in experiments. According to results, fretting fatigue life of the substrate material was dependent on the pad material. The fretting fatigue lives were examined under both high cycle and low cycle fatigue regimes. It was observed that friction force carrying capacity of aluminum pad was higher than steel pad load carrying capacity. In the second part of the study, finite element analysis was performed. The crack initiation lives and crack propagation lives were calculated using finite element model. According to results, fretting fatigue lives were obtained from finite element analysis were close and had similar trend with fatigue lives obtained from the experiments.

Keywords: Fretting fatigue, Contact mechanics, Finite element analysis, Dissimilar materials, Fatigue life

# ÖZ

## FARKLI MALZEMELERİN TEMAS YÜZEYLERİNDEKİ TİTREŞİMLİ AŞINMA YORULMASININ TEST VE NÜMERİK OLARAK İNCELENMESİ

Korkmaz, Yezdan Medet
Yüksek Lisans, Havacılık ve Uzay Mühendisliği
Tez Danışmanı: Doç. Dr. Demirkan Çöker

Eylül 2019, 93 sayfa

İlk kısımda farklı malzemeler temas halindeyken titreşimli aşınma yorulma durumunun ilgilenilen malzeme üzerindeki etkisini yorulma ömrü, sürtünme kuvveti ve temas yüzeyleri açısından görebilmek için farklı temas malzemeleri kullanılarak yorulma testleri gerçekleştirildi. Testlerde aşındırma yapısı için çelik ve alüminyum malzemeleri kullanıldı. Test sonuçlarına göre aşındırılan malzemenin yorulma ömrü aşındırma yapısı için kullanılan malzemeye bağlı olduğu görüldü. Titreşimli aşınma yorulma test sonuçları, yüksek ve düşük çevrimli yorulma durumları için incelendi. Aşındırma yapısı için alüminyum malzemesi tercih edildiğinde aşındırma yapısı üzerinde taşınan sürtünme kuvveti değerinin çelik malzeme kullanılarak yapılan testlere göre daha yüksek olduğu görüldü. Çalışmanın ikinci kısmında sonlu elemanlar analizi yapıldı. Sonlu elemanlar modeli kullanılarak çatlak başlama ömrü ve çatlak ilerleme ömürleri hesaplandı. Sonuçlara göre sonlu elemanlar analizi ile bulunan titreşimli aşınma yorulma ömrü ile testlerden bulunan yorulma ömürlerinin birbirine yakın ve benzer trend içerisinde bulundukları görüldü.

Anahtar Kelimeler: Titreşimli aşınma yorulması, Temas mekaniği, Sonlu elemanlar analizi, Farklı malzemeler, Yorulma ömrü

To my family

## ACKNOWLEDGEMENTS

Firstly, I would like to express my sincere gratitude to my advisor Assoc. Prof. Dr. Demirkan Çöker for his continuous support of my MSc study and related research for his patience, motivation, and immense knowledge. His guidance helped me in all the time of research and writing of this thesis. Besides my advisor I would like to thank the rest of my thesis committee.

I would like to thank my team leader, Evren Eyüp Taşkınoğlu and my collegues, Fatih Özbakış, Namık Kemal Alpaydın, Berkay Özkan, Yasin Karasu, and Haydar Dirik in for the stimulating discussions, motivation and for all the fun we have had. Also, I thank my friends Tuğba Şimşek, Ali Yücel Türegün, and Ersin Gül for their patience, motivational speeches and supports.

I would like to thank Emine Burçin Özen who were involved in evaluation of the experimental results. My sincere thanks also go to Yusuf Ulu, Şahin Gören, Salim Çalışkan, Çağrı İlhan and Ozan Mert Türkatar for their support and contribution to experiments.

I am greatly thankful to Turkish Aerospace for their valuable support.

## TABLE OF CONTENTS

## LIST OF TABLES

TABLES

## LIST OF FIGURES

FIGURES

# CHAPTER 1

# INTRODUCTION

The main objective of this study is to investigate the effect of the fretting phenomenon between dissimilar mating surfaces under the same normal load in terms of fatigue life of the AL7050 T7451 aluminum alloy, a material frequently used in the helicopter industry. In this regard, fretting fatigue experiments with cylinder on flat contact configuration have been performed in order to figure out the impact of fretting on the reduction of the fatigue life of the material. T7451 and 15-5PH steel were chosen as mating materials so as to capture the effect of material dissimilarity. The results of these experiments were compared in terms of fretting fatigue lives, friction force on the substrate material, and the appearance of contact surfaces. In order to crosscheck the findings of the experiments and sort out a model to be used for further materials, finite elements simulations have been additionally carried out. Later, the fatigue life obtained from the finite elements simulations and the experiments have been compared.

A fretting phenomenon is defined as a small sliding movement in the contact surface that occurs between two contacting bodies. Fretting is generally classified as fretting fatigue or fretting wear depending on the relative sliding between the contacting bodies both of which lead to failure by fatigue. Fretting fatigue incurs more detrimental effects than fretting wear on contacting areas since small cracks, which result from cyclic small sliding in the contacted region, are removed due to fretting activities [1]. The life relation between fretting fatigue and fretting wear is given in Figure 1.1.

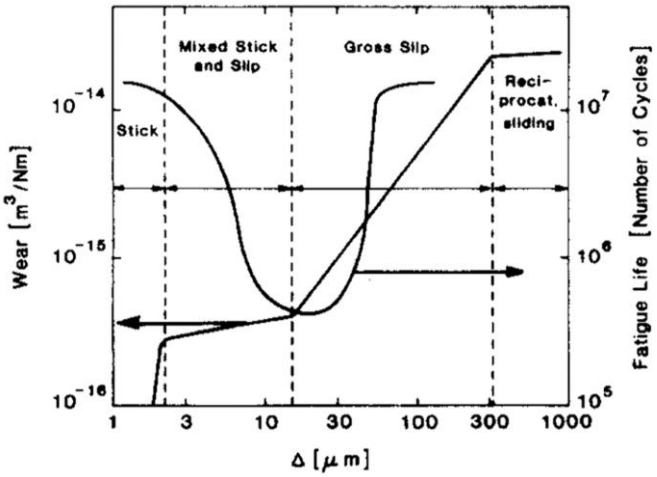


Figure 1.1. Schematic illustration of the variation in fretting fatigue life and fretting wear rate with displacement amplitude [1]

The first observation of the fretting phenomenon was made by Eden et al. on a steel specimen surface contacting with steel grips in the form of brown oxide debris [2]. Fretting phenomenon can be observed on a variety of parts such as bolted joints and lug attachments of aircraft structures, dovetail joints in aircraft engines, gas turbines, wire ropes and ball bearings [3-7].

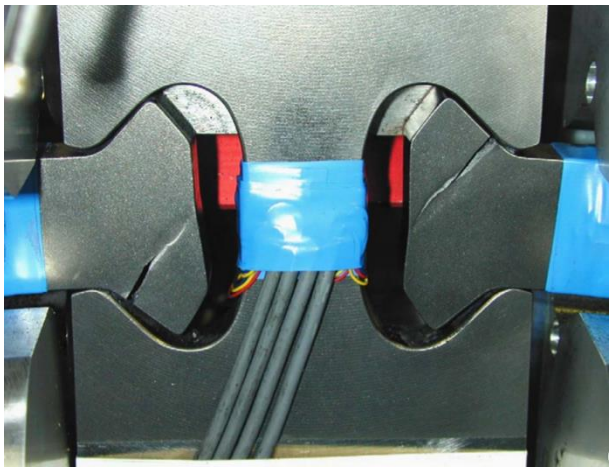

Figure 1.2. Failure in dovetail joint due to fretting [5]

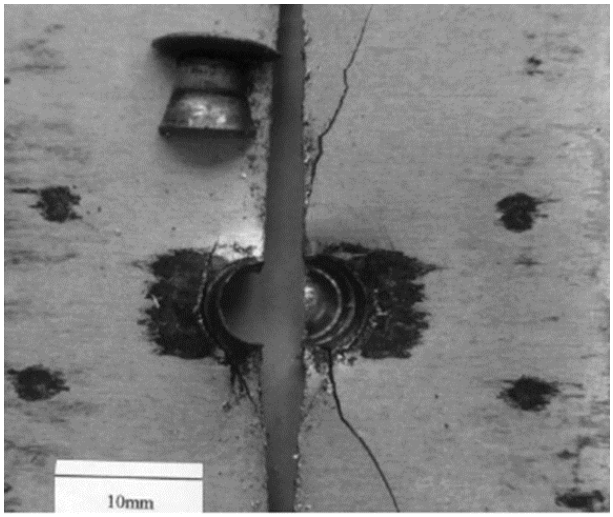


Figure 1.3 Fretting scars on the surface of the riveted plate [6]

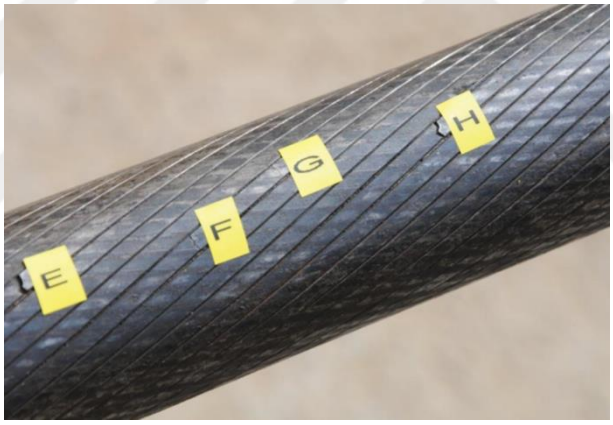


Figure 1.4. Cracks on the wire rope due to fretting [7]

Small cyclic loading leads to fretting between the contacting bodies, which creates stick and slip regions in the contact area. It is generally observed that stick region lies at the center of the contact area and that slip regions occur at the edge of the contact area. Nicholas [8] states that the stick region implies an area of the contact in which no relative displacement is observed and the remaining portion, where displacement occurs, is called the slip region. The relative displacement in the slip region leads to

surface deterioration. The rate of damage on the contact surface depends on the material and geometric shapes of the contacting bodies. According to fretting experiments performed by Warlow-Davies [9], the endurance limit of the fretted steel specimens is lower than that of unfretted fatigue test specimens.

In order to examine the fatigue failure of materials due to fretting, great numbers of coupon or component level experiments have been performed in the literature. A large portion of the fretting fatigue studies examines the effect of fretting on the crack nucleation in the contact region [10-12] and fatigue strength reduction with no emphasize on mating material similarity [13]. Some studies were performed to clarify the parameters which affect the experiments and analyses. Adibnazari and Hoeppner [14] examined the effect of the contact pressure on the endurance limit of the materials by performing fretting fatigue experiments at different contact pressure values. Their results indicated that the endurance limit of a material is independent of normal pressure after a certain value. The relation between the fretting fatigue life of the material and applied normal pressure is given in Figure 1.5.

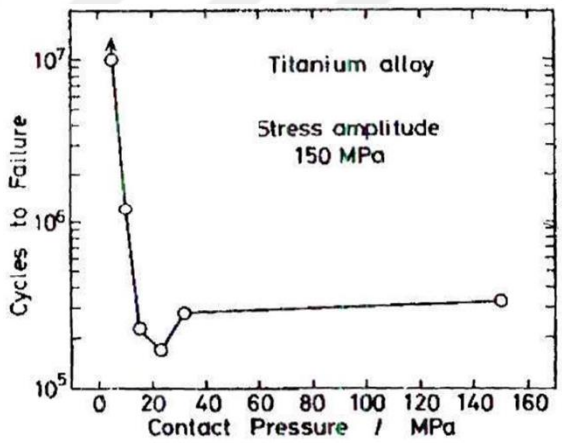


Figure 1.5. Effect of contact pressure on the fretting fatigue life of Ti-6Al-4v [15]

As mentioned before, even though many studies have been devoted to the exploration of the fretting phenomenon, most of them have focused on contacting bodies that have similar materials. However, in industry, and especially in the aerospace industry, there are many instances where parts contain contacting dissimilar materials such as

dovetail joints, and riveted and bolted joints; rendering it crucial to investigate the fretting phenomenon between dissimilar bodies. In the scope of this study, fretting fatigue experiments of dissimilar mating materials have been carried out. While there are many opportunities for research to investigate fretting occurring between dissimilar contacting surfaces, there are some studies in the literature that have addressed some aspects of this issue. A significant insight in this regard can be obtained from the study of Lindley and Nix [16], who conducted fretting fatigue experiments using NiCrMoV rotor steel as a substrate material. They concluded that while different fretting scars are formed on the contact region due to different pad materials, fretting fatigue life of the material does not change significantly. Similar conclusions were also obtained by others [17,18]. According to Lykins et. al. [19], the fretting fatigue life of Ti-6Al-4V titanium alloy is independent of the pad material under the same Hertzian contact pressure. Even though these studies have examined the fretting phenomenon on dissimilar mating materials, it can still be claimed that aluminum-aluminum and aluminum–steel interaction and comparisons have continued to be overlooked. Deriving from this point, in this study, the material of interest has been chosen as AL7050 T7451 aluminum alloy and the mating materials have been identified as 15-5PH steel and AL7050 T7451 aluminum alloy.

Generally, the fretting fatigue life of the material is composed of crack initiation life and propagation life [20]. Thus, fretting fatigue life of the analyzed body, calculated by crack initiation and crack propagation life approaches where the stress state of the substrate material was determined with finite element simulations [21-24]. To obtain the crack nucleation location and to calculate crack initiation life accurately, multiaxial fatigue theories have been employed since a multiaxial stress field exists around the contact area. Various multiaxial fatigue methods exist in the literature: namely empirical, stress invariant, critical plane and mesoscopic [25,26]. Sum et al. [27] used Smith-Watson-Topper (SWT), which is a critical plane approach, to determine the fretting fatigue life of the spline couplings and compared their results with test results. Lykins et al. [19] stated that SWT and maximum shear stress range

(MSSR) critical plane parameters are capable of predicting the crack nucleation location and initiation life of titanium alloys. Neu et al. [28] performed fretting fatigue analysis using both traditional and critical plane theories including SWT and Fatemi-Socie (FS) approaches and compared the results with each other. Their results indicate that the FS approach leads to more accurate determination of the crack initiation location compared to other approaches.

To estimate the total life of the substrate material, it is also crucial to calculate the crack propagation life. Often in the literature linear elastic fracture mechanics (LEFM) is used to calculate the fretting fatigue crack propagation life [29-31]. To use fracture mechanics approach, the stress intensity factor (SIF) at the fretting fatigue crack tip should be known at each crack increment. Weight function [32-34] approaches as well as conventional and the extended finite element method [35-38] are used to calculate SIF values during the crack propagation process. Although the former is a cost-effective method, it does not allow the inclusion of the contact between the crack faces in the SIF calculation process [39]. While the finite element method requires excessive effort and time, it is more precise in terms of the crack propagation path and allows for the contact between the crack faces.

In order to see whether simulations offer accurate and reliable results, they need to be compared with experiments, which has also been the attempt of this study. During the experiments, test setups have the utmost importance in order to obtain reliable results. Test setup selection in fretting fatigue studies is not only critical, but also the initial step of the studies. Various fretting fatigue test setups exist in the literature, such as one-actuator or two-actuator test rigs [40,41]. Experiments are also performed with rotating-bending test machine [42]. Usually, the fretting fatigue test methods are classified with respect to the contact condition between the mating surfaces as either a complete (flat-on-flat) or incomplete (cylinder-on-flat) contact [43-50]. Flat pads are needed to achieve flat-on-flat contact methods. It is crucial to define stick-slip zones on the contact area when flat-on-flat contact conditions are employed [51]. Pape and Neu [52] examined the behavior of complete and incomplete contact conditions by

using these conditions simultaneously in their test apparatus. They observed that the contact configuration affects the early damage formulation on the contact area.

Deriving from the aforementioned points, the objective of this study can be reframed as to investigate the effect of dissimilar mating materials to the total fatigue life under fretting fatigue conditions using finite element method under the same applied normal load and compare the results observed from fretting fatigue experiments.

In Chapter 2, fretting fatigue experiments with cylindrical on flat contact configuration are performed in order to examine the effect of the dissimilar mating materials. Al7050 T7451 aluminum alloy is selected as a testing material which is a material frequently used in the helicopter industry. As a mating material Al7050 T7451 and 15-5PH steel are selected. The experiments are designed to compare the effect of similar and dissimilar mating materials. Additionally, the change in the frictional force variation during the experiments are examined. The frictional force carrying capacity is obtained for each pad material. The contact surfaces and crack faces on the specimen are observed for both pad materials. Results are compared with unfretted fatigue results in both high cycle and low cycle fatigue regimes. The results show that dissimilar mating materials change fretting characteristics and reduce the fatigue life of the substrate material. In addition, under the high cycle regime fretting fatigue results in further detrimental effects on the fatigue life of the substrate materials.

In Chapter 3, the fretting fatigue life of the contacting material is calculated using analytical methods in conjunction with the finite element method to compare the results of the experiments to simulation studies. These types of comparison are crucial value to many industrial applications since in many cases experimentation is demanding. In the analysis, the fatigue lives of the materials are calculated by summing the initiation and propagation lives. For the initiation life calculation, Fatemi-Socie multiaxial fatigue criteria is utilized. The crack propagation phase is accomplished by using both the Seam crack methodology via ABAQUS$^{TM}$ and the weight function method. Linear elastic fracture mechanics approach methodology is

used in the calculation of crack propagation life. The contact condition in the fretted area is investigated with finite element results. Results are calculated by employing numerical approaches and are then compared with the experimental result. To clarify the effect of the fretting fatigue in terms of fatigue life, fatigue strength reduction factors are calculated and compared to each other. The fatigue life simulation results are then compared with the experiment results.

In Chapter 4, the findings that are presented in Chapters 2 & 3 are discussed in length. In addition, the error of finite elements is also measured in terms of the reduction factor calculated from the experiments and simulations.

Lastly, in Conclusion, a brief overview of the whole study is presented and the particular contribution of this thesis to the existing literature is mentioned.

# CHAPTER 2

# FRETTING FATIGUE EXPERIMENTS

In this chapter, fretting fatigue experimental test setup is designed and built. The fretting fatigue experiments are done in order to examine the effect of dissimilar mating materials. Al7050 T7451 aluminum alloy is selected as a testing material which is a frequently used material in the helicopter industry. As a mating material Al7050 T7451 and 15-5PH steel are selected.

## 2.1. Experimental Setup

Bridge type fretting fatigue test setup is designed and used in this investigation. A schematic representation of the bridge type test configuration including the specimen, fretting pads, pad loaders, cylindrical pins and strain gages on the fretting pads are shown in Figure 2.1. A dog-bone specimen with a rectangular cross-section is used with the fretting pads which apply a normal load on the two thinner sides of the specimen. At the beginning of the experiment, the normal load is applied and maintained at the desired value corresponding to the required contact pressure level. Then, the bottom side of the specimen is constrained in a wedge grip and a cyclic axial load is applied to the top of the specimen until the specimen fails.

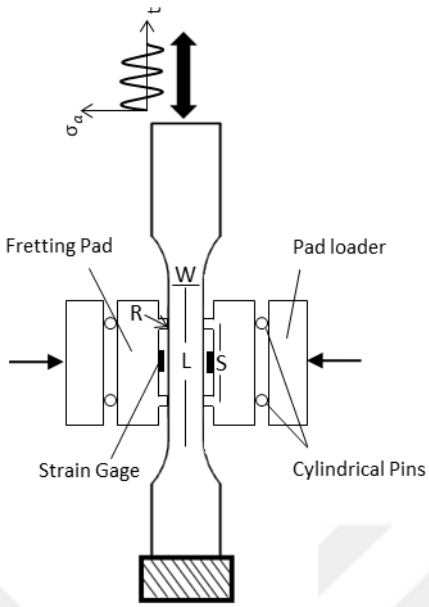


Figure 2.1. Representative view of the bridge type fretting fatigue experiment showing the dogbone specimen and the two attached pads

For this experiment, $S$=10mm is the pad span, $L$=57 mm is the length of the specimen, $W$=12,5 mm is the width of the specimen and $R$=50 mm is the radius of the pad feet. The CAD drawings of the fretting pad, proving ring and the specimen are given in Appendix A. In order to reduce the bending on the pads, the normal load should be distributed equally to each fretting pad feet. To achieve this, two steel cylindrical pins are located between each fretting pad and pad loaders. Extension and bending in the fretting pad represent the friction force between pads and the specimen. A strain gage is located under each fretting pad to measure the friction force variation during the experiment.

The experimental setup consists of fretting pads, bolts, adjusting screws, pad loaders, cylinder pins, proving ring and springs. A photograph of the setup used in this experiment is provided in Figure 2.2. A circular proving ring is used to transmit the normal load to each pad equally. To assemble the specimen into the test apparatus, one of the fretting pads is in contact with the specimen at the center of the circular proving ring. Then, the other fretting pad is pressed to the specimen using adjusting

screws and bolts on the proving ring. The adjusting screws are used to fix the normal load at a constant value during the test. The proving ring apparatus is not connected to the test machine and only rests on the specimen.

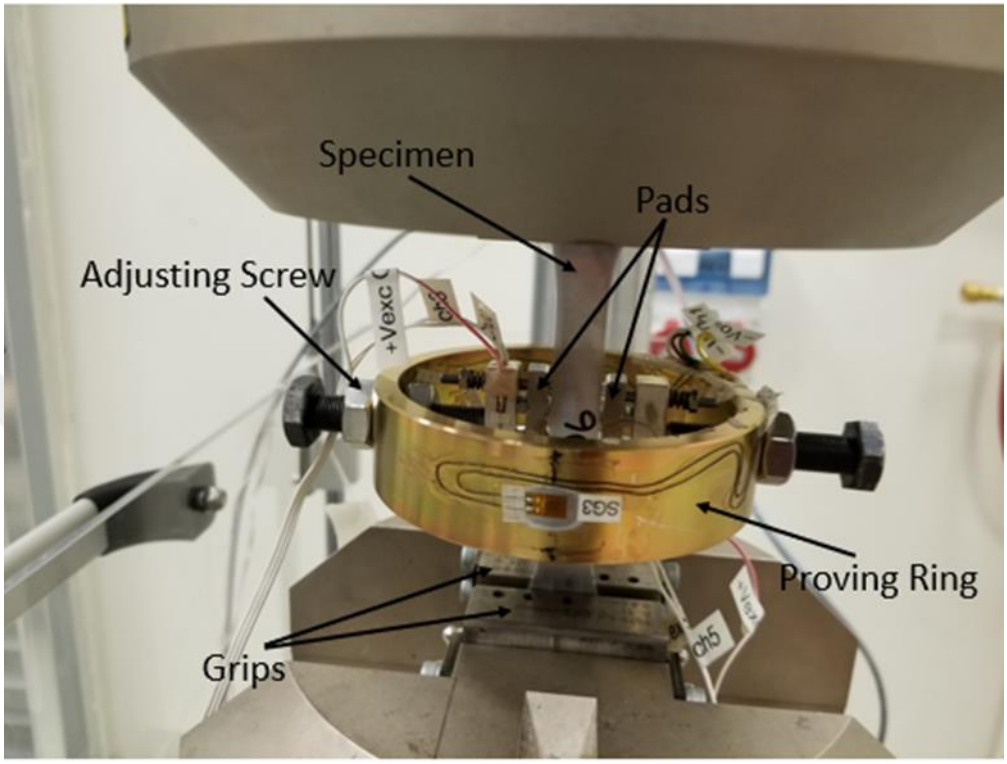


Figure 2.2. Fretting fatigue experiment set-up

In order to check the accuracy of the applied loads and the change in the friction force during the test, strain gages are located on the proving ring (shown in Figure 2.2) and fretting pads (shown in Figure 2.1). Two strain gages are attached in the inner and outer circumference of the proving ring structure on both sides perpendicular to the bolted sides. As mentioned before, a strain gage is attached to the bottom side of each fretting pad. The normal load is measured during the experiments with strain gages on the proving ring. The strain gage under the bottom side of the fretting pad is used to determine the friction force variation during the test as explained in the calibration section. Calibration tests are required to measure the correct normal force and to relate the strain readings on the fretting pads.

The test apparatus is only constrained to the specimen using a normal force via the fretting pads. Thus, the weight of test apparatus should be as small as possible to reduce its inertia [53]. The frequency to be used for cyclic loading has a significant effect on the test results. In tests that take place at high frequencies, the temperature at the contact area affects results. To reduce this risk, the test should be performed at low frequencies. The testing environment for the experiments conducted for this study consisted of standard laboratory conditions within a temperature range of 21-24 C. A constant amplitude cyclic fatigue loading is applied to the specimen at a frequency of 5 Hz.

The fretting fatigue tests were conducted on an Instron servo-hydraulic fatigue test machine in Turkish Aerospace. After the specimen was gripped with the hydraulic wedge grips, the fretting apparatus was assembled together with the specimen carefully. Strain gage data were recorded with an acquisition rate of 128 points per second. Five tests were conducted for each Al7050 T7451 aluminum and each 15-5PH steel pads on an Al7050 T7451 aluminum specimen. A constant normal load of 3000 N was applied in all tests whereas the fatigue stress varied for each test with a load ratio of R = - 1. The test was stopped once failure occurred where failure can be defined either as a complete separation or as a loss of load carrying capacity. S-N diagrams and friction force hysteresis curves were constructed as a result of these tests.

### 2.1.1. Calibration Tests

Calibration tests should be performed (a) to measure the applied normal load on the specimen and (b) to calculate the friction force during the experiments. For part (a), proving ring calibration is achieved by constraining one side of the ring and applying axial force to the other side of the structure in the direction of compression (see Figure 2.3). This calibration test makes it possible to set a relation between the applied load and the measured strain on the proving ring structure.

Figure 2.3. Proving ring calibration setup

For part (b), to relate friction forces to the strain gage measurement on the fretting pads, calibration tests are required to include both the extension and bending of the fretting pads. To relate the friction force to the strain gage reading between the two feet of the pads, a split specimen technique is used as shown in Figure 2.4.

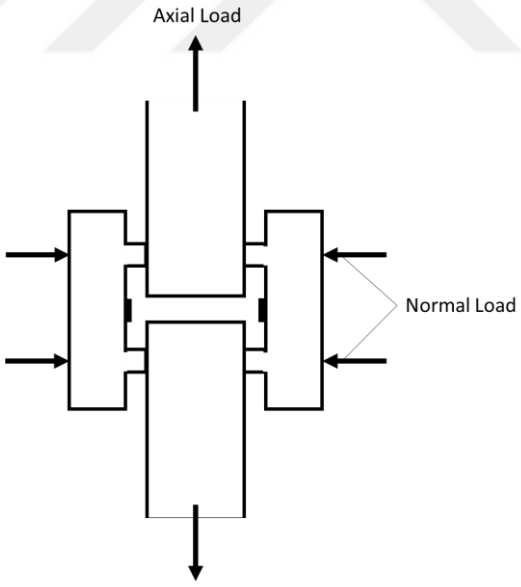


Figure 2.4. Schematic representation of the split specimen setup

The applied axial load on one piece of the specimen is transferred to the other part of the specimen only through the fretting pads during this test [54]. The friction force transmitted by the pads is measured by the strain gages on the pads. A relationship is constructed between the transferred load and the measured strain under the fretting pads as explained in Figure 2.5.

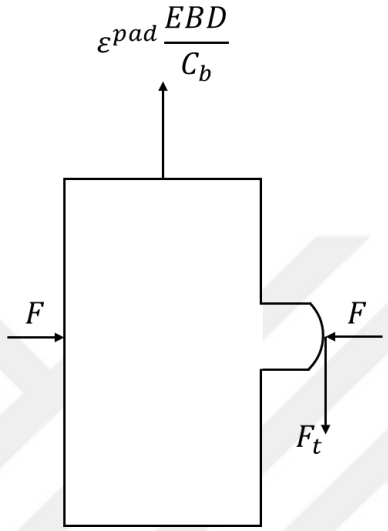


Figure 2.5. Free Body Diagram of fretting pad during the calibration test

The frictional force is calculated from the measured strain using

$$F_t = \varepsilon^{pad}\frac{EBD}{C_b} \tag{2.1}$$

where $E$ is the elastic modulus of the material, $\varepsilon^{pad}$ is the strain at the bottom surface of the pad, $F_t$ is the frictional force, $B$ and $D$ are the pad thickness and height respectively, and $C_b$ is calculated from the applied axial force-measured strain calibration curve. $C_b$ is used to include the extension and bending of the fretting pad in the calibration equation. The calibration curve of the aluminum-aluminum contact condition is shown in Figure 2.6.

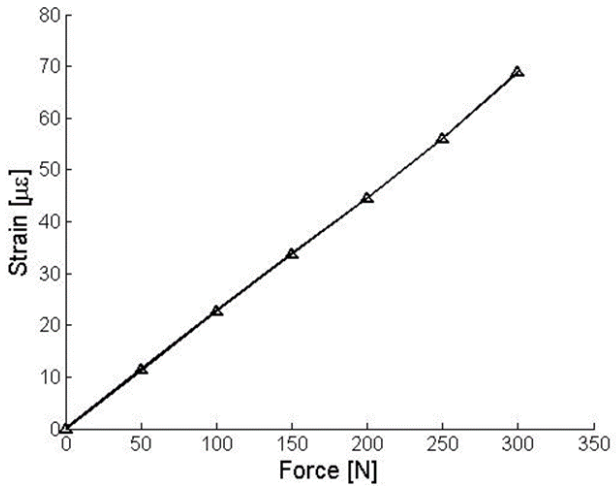


Figure 2.6. Calibration curve of the split specimen test for aluminum-aluminum contact

The calibration tests were performed two times for each fretting pad. The average bending correction factors are obtained as 1.654 (aluminum-aluminum contact) and 4.628 (steel-aluminum contact).

If friction is ignored at the contact region, then entire applied axial load is transmitted through the specimen. The relative slip range for frictionless contact is given by,

$$\sigma_a = \varepsilon_a E, \tag{2.2}$$

$$\sigma_a = \frac{\delta_n}{S} E, \tag{2.3}$$

$$\delta_n = \frac{\sigma_a}{E} S, \tag{2.4}$$

where $\sigma_a$, S and E are the normalized axial cyclic stress amplitude, fretting pad span, and elastic modulus, respectively. To include the friction between the pad and the specimen, the relative strain on the specimen should be corrected by adding the measured strain from the fretting pads. As such, the relative slip range equation including the friction becomes,

$$\delta_n = \left(\frac{\sigma_a}{E} - \varepsilon_a^{pad}\right) S, \tag{2.5}$$

where $\frac{\sigma_a}{E}$ and $\varepsilon_a^{pad}$ are the bulk specimen axial strain amplitude and fretting pad extensional strain amplitude, respectively.

### 2.1.2. Material

The material of the fretting fatigue specimen is AL7050 T7451 aluminum alloy. The materials of fretting pads are AL7050 T7451 and 15-5PH steel. The material properties of AL7050 T7451 aluminum alloy shown in Table 2.1. Young modulus and poisson ratio of 15-5PH steel are 197GPa and 0.27 [55], respectively. The surface roughness of the pad and specimen is 1.6.

Table 2.1. Material properties of AL7050 T7451 [53-55]

| Properties | Values |
|---|---|
| $E$ | 71 GPa |
| $\nu$ | 0.33 |
| $\sigma'_f$ | 839 MPa |
| $b$ | -0.1083 |
| $C$ | 1.53E-10 |
| $m$ | 2.5 |

## 2.2. Results

### 2.2.1. Fretting Fatigue Lives

In this section, the results of the 10 experiments are presented. Applied axial cyclic stresses are different in each test. The normalized axial cyclic stresses as well as the total relative displacement between the specimen and the pad ($\delta_n$), the steady normalized frictional force value, $Q$, at the maximum value of the applied normalized cyclic load and the fatigue life are shown in Table 2.2 and Table 2.3 for steel pads and aluminum pads, respectively. Due to complications that occurred during the experiments no displacements were obtained for the tests 4 and 5. All fretting specimens failed with the exception of one. Tests were performed to cover both the low cycle and high cycle regimes in order to obtain the effect of the fretting in terms of the fatigue life of the specimen. No failure was observed in the fretting pads.

As shown in Table 2.2 and Table 2.3, relative slip values are found to be higher for the same normal load when the steel pad is contacted with the aluminum specimen instead of the aluminum pad. This result implies that the aluminum-aluminum contact condition has a higher friction coefficient condition than the steel-aluminum contact condition.

Table 2.2. Experimental results of the steel pad

| Test | $\sigma_a$[-] | $\delta_n[\mu m]$ | $Q$[-] | $N$[Cycles] |
|---|---|---|---|---|
| 1 | 2.72 | 18.35 | 0.5 | 30,096 |
| 2 | 1.82 | 12.33 | 0.3 | 182,663 |
| 3 | 1.27 | 8.92 | 0.2 | 499,286 |
| 4 | 1.0 | - | - | 1,442,322 |
| 5 | 1.27 | - | - | 735,233 |

Table 2.3. Experimental results of the aluminum pad

| Test | $\sigma_a$[-] | $\delta_n[\mu m]$ | $Q$[-] | $N$[Cycles] |
|---|---|---|---|---|
| 6 | 1.82 | 10.89 | 0.55 | 295,518 |
| 7 | 1.27 | 7.86 | - | Run-out |
| 8 | 1.63 | 9.51 | 0.5 | 538,580 |
| 9 | 2.72 | 15.48 | 0.9 | 69,143 |
| 10 | 2 | 11.79 | 0.62 | 220,223 |

In addition, the fretting fatigue life is found to be dependent on the pad material for the same normal load. It is observed that experiments executed with steel pads result in lower fatigue lives in both low cycle and high cycle regimes. These results show that the stiffer the pad material is, the shorter the fretting fatigue life.

Figure 2.7 shows the S-N curves of AL7050 t7451 specimen for fretting fatigue with aluminum and steel pads and the unfretted fatigue results of the same materials. The plain fatigue life tests were conducted according to MMPDS [55]. The circles and squares represent the fretting tests and the triangular symbols represent the plain fatigue results. The life is seen to decrease significantly for the fretting conditions as compared to plain fatigue, reduced as much as 10 times in terms of cycles.

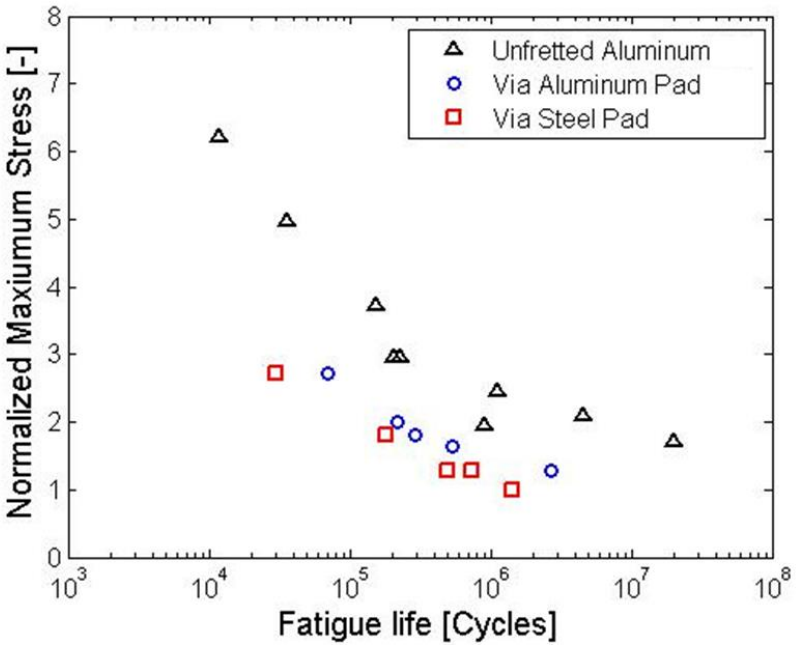


Figure 2.7. S-N curves of AL7050 t7451 specimen for fretting fatigue with Al and Steel pads and plain fatigue

A photograph of failed specimen 6 after 295,518 cycles is shown in Figure 2.8. The normalized applied axial cyclic stress is 1.82 for that experiment. There was only one primary crack that appeared in the specimen and the crack nucleation point was in the contact area. It is observed that the crack initiation point occurred at the trailing edge of the contact area which refers to the side of the specimen close to the applied axial stress. The leading edge, the opposite side of the trailing edge, is the side where the boundary conditions are applied. The results are aligned with those found by Szolwinski and Farris [58].

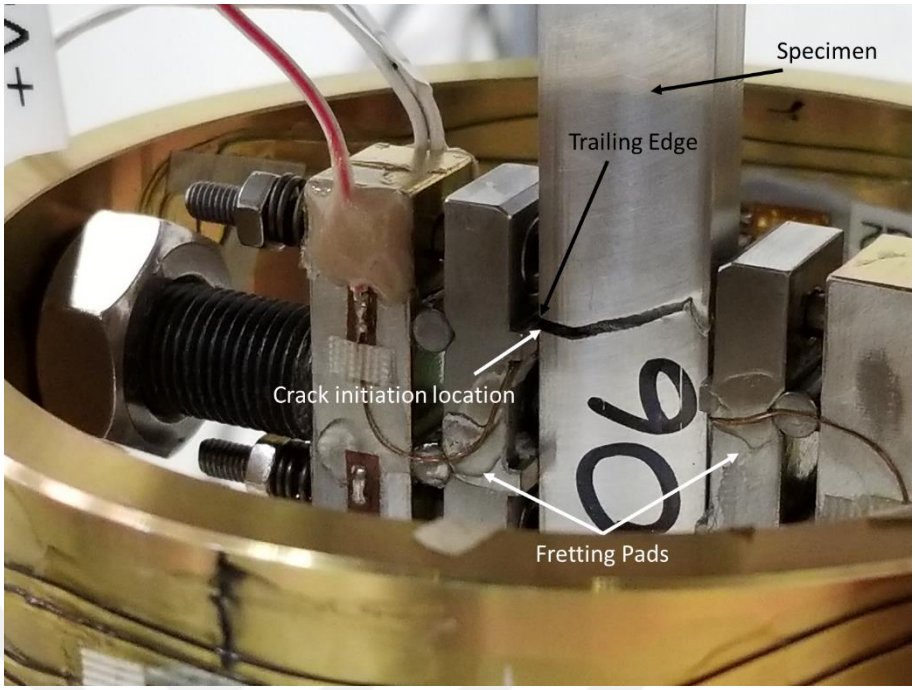


Figure 2.8. Failed specimen during the experiment

### 2.2.2. Frictional Force Measurements

Frictional force measurements are another key step in the analysis since it is necessary to understand how the pad material affects the friction force and how the friction force changes during the experiments. The evolution of frictional force ranges over the cycles as well as the hysteresis of frictional force versus load applied to the fatigue specimen are useful for quantitatively characterizing how damage evolves during the test. Contact conditions during the experiment can be used to extract information regarding gross slip or partial sliding. The friction force variation curves are given in Appendix B.

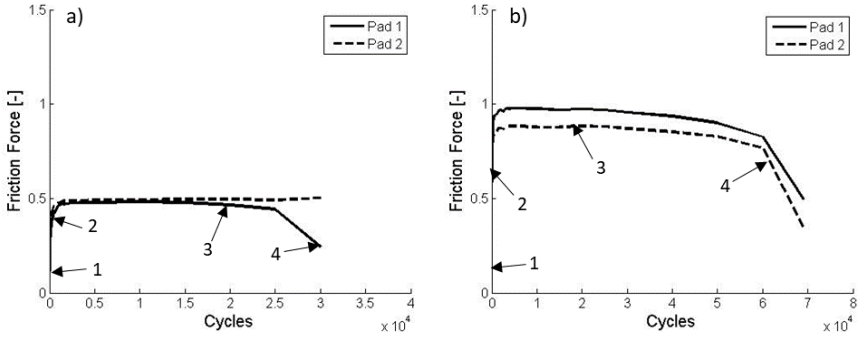


Figure 2.9. Variation of normalized frictional force during (a) test 1 (Pad=15-5PH, R=-1, $\sigma_a$ =2.72, N=30096 Cycles) (b) test 9 (Pad= AL7050 T7451, R=-1, $\sigma_a$ =2.72, N=69143 Cycles)

In Figure 2.9, the normalized frictional force variations during test 1 and test 9 were compared since these two tests were performed for the same axial cyclic stress but used different pad materials. The black and dashed lines imply the frictional force variation in both pads. The frictional force is normalized with the maximum friction force, which is measured during the experiments.

The frictional force variation for test 1 is shown in Figure 2.9a. The pad material is 15-5PH steel. The normalized applied axial cyclic stress is 2.72. The specimen failed after 30,096 cycles. According to Figure 2.9a, frictional force begins to fall after 20000 cycles in one of the pads, whereas the frictional force stays constant on the other pad. This change in frictional force is the result of crack nucleation at the contact area. The crack nucleated at one side of the specimen according to Figure 2.9a. The acceleration of the frictional force reduction depends on the crack length. After 25,000 cycles, it can be seen that the frictional force decreases dramatically which leads to the conclusion that the crack length increases during this time. At the 30,096 cycle, the specimen failed and the friction force became zero.

The frictional force variation for test 9 is shown in Figure 2.9b. The pad material is AL7050 T7451 aluminum. The normalized applied axial cyclic stress is 2.72. The specimen failed after 69,143 cycles. The friction force remains unchanged up until 20,000 cycles, after which the friction force decreases gradually in both pads. This reduction is due to crack growth on both sides of the specimen. After 60,000 cycles,

the friction force decreases rapidly in both contact regions which implies that the crack propagation rate increases after these cycles. The specimen failed on the 69,143 cycle.

To explore the effect of different pad, test 1 and test 9 results were compared. It is observed that the frictional force increases immediately within the first hundred cycles in both tests. After a certain number of cycles, the frictional force reaches steady value. It is observed that these steady values are different for each pad, even though the same loads were applied in both experiments. The frictional force in test 9 (Figure 2.9b) is nearly two times higher than the measured frictional force in test 1 (Figure 2.9a). As a result, it can be concluded that the aluminum-aluminum contact condition has a higher friction coefficient than the steel-aluminum contact condition.

The normalized frictional force values, Q, for steady state condition are shown in Table 2.2 and Table 2.3. These frictional force values are determined by averaging frictional forces measured from each pad in each test. The frictional forces are compared in order to observe the effect of the axial cyclic load on the frictional forces occurring on the same pad material. The axial cyclic loading applied in test 9 is higher than that of test 6. The result implies that the friction force transmitted from the specimen to the fretting pads is not only dependent on the pad material but also depends on the magnitude of the axial cyclic loading. There is a direct proportion between the axial load and frictional force.

Hysteresis curves are necessary to identify the contact conditions and their variation throughout the experiments. The hysteresis curves of frictional force versus applied load can be characterized as one of three typical shapes; namely, representing a stick, partial slip, or gross slip condition. All of which can be seen in Figure 2.10. Under stick conditions (Figure 2.10a), there is no relative slip between contacting parts. In addition, there is no visible damage to the contact area. Under partial slip conditions [1] (Figure 2.10b), part of the contact region undergoes slip during the axial loading cycle of the specimen causing an elliptical type hysteresis curve. Under gross slip

(Figure 2.10c), the bodies completely slip with respect to each other and the resulting hysteresis is shaped more in the form of a square.

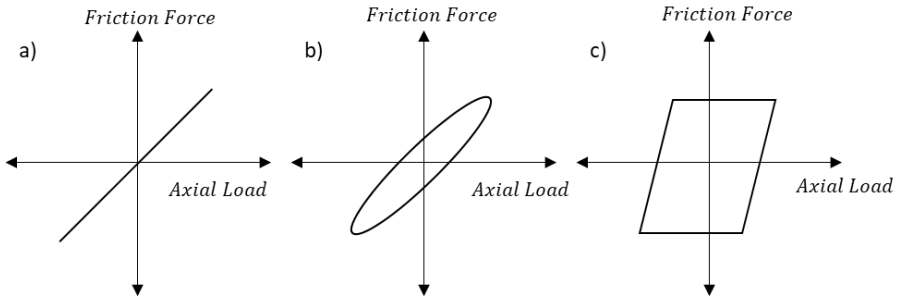


Figure 2.10. Types of frictional force hysteresis loops

Frictional force vs. applied normalized cyclic load hysteresis loops for test 1 (steel pad material, $\sigma_a = 2.72$) are given in Figure 2.11 at different cycle numbers. The specimen failed after 30,096 cycles. In Figure 2.11a, the first cycle of the experiment is shown. In Figure 2.11b, the frictional force vs. applied load hysteresis loop is represented after 500 cycles. Figure 2.11c shows the change in the frictional force after 20000 cycles and Figure 2.11d represents the experiment after 30000 cycles. The location of these hysteresis loops with respect to the frictional force variation curve is shown in Figure 2.9a.

It is obvious that at the first cycle of test 1 that a relative displacement existed between the contacting faces, which means that a gross slip condition exists between the pad and specimen. In addition, there is a difference in frictional forces between the two pads which may have occurred due to the misalignment of the pads, and both of the pads carry nearly the same frictional load after a certain cycle. After a certain number of cycles, the contact condition changes between the pad and the specimen. The gross slip condition turns into a partial slip condition which means that stick and slip regions exist in the contact region. This process is also known as bedding-in-phase in literature [59]. The bedding-in-phase consists of a gradual build up in the magnitude of the frictional forces and a reduction in the degree of macroslip. This was equated to wearing away the larger contacting asperities, during which macroslip occurred, and

to increasing the area of the asperity of contact, which promoted microslip conditions. After bedding-in-phase the frictional force remains nearly constant during the test until the crack initiates under the contact area. The contact condition between the pad and specimen still falls under the partial slip condition at cycle 20,000. Besides, there is no evidence indicating the initial crack up to 20,000 cycles according to Figure 2.11c. According to Figure 2.11d, there is a crack at the contact area. However, the crack only occurs on one side of the specimen, whereas the other pad still carries the friction force which can also be observed by comparing the two dashed lines in the same figure. The effect of the crack can be seen when the cyclic axial load is in tension. Figure 2.11 also shows that the crack does not result in any effects when the cyclic load is compressed.

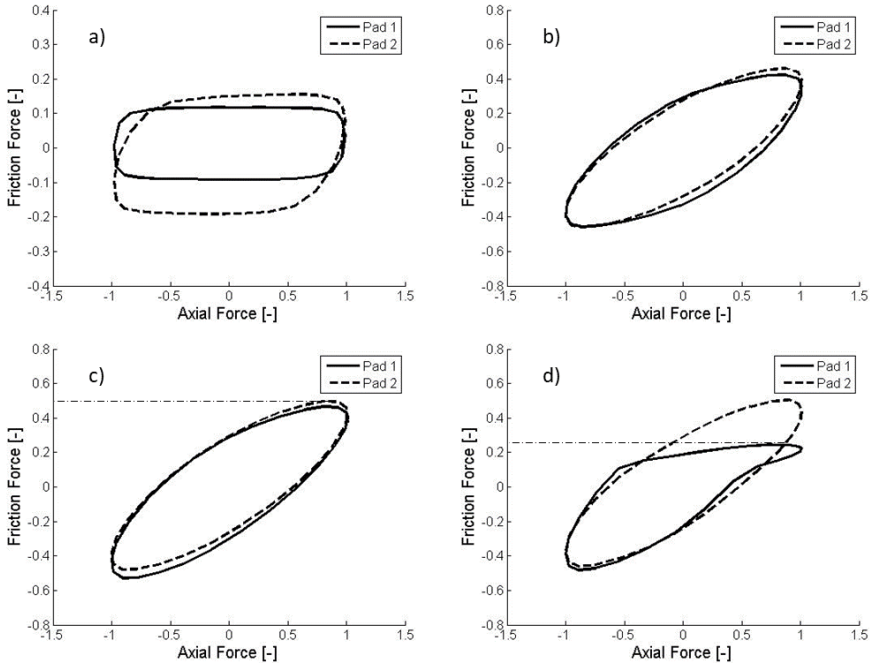


Figure 2.11. Frictional force-applied load hysteresis loop for test 1 (Pad=15-5PH, R=-1, $\sigma_a = 2.72$, N=30096 Cycles) at (a) cycle 1, (b) cycle 500, (c) cycle 20000, (d) cycle 30000

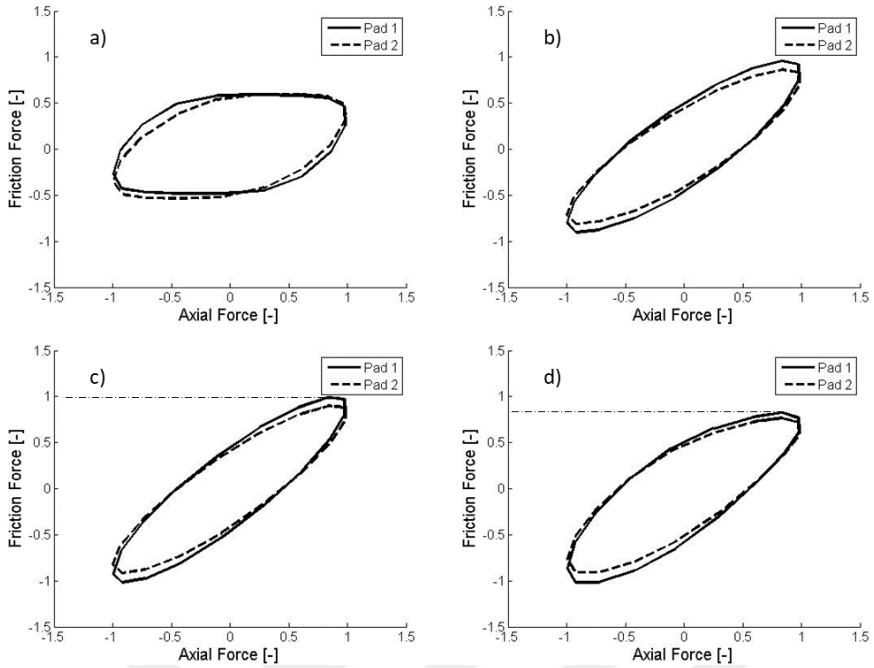


Figure 2.12. Frictional force-applied load hysteresis loop for test 9 (Pad=AL7050 T7451, R=-1, $\sigma_a = 2.72$, N=69,000 Cycles) at (a) cycle 1, (b) cycle 500, (c) cycle 20,000, (d) cycle 60,000

The frictional force vs. applied axial load hysteresis loops for test 9 (aluminum pad material, $\sigma_a = 2.72$) are given in Figure 2.12. The specimen failed after 69,000 cycles. The first cycle of the experiment is shown in Figure 2.12a. The frictional force hysteresis loop after 500 cycles is given in Figure 2.12b. Changes in the frictional force after 20,000 cycles and 60,000 cycles is represented in Figure 2.12c and Figure 2.12d, respectively. The points represented by numbers 1,2,3, and 4 in Figure 2.9b refers to the hysteresis loops a, b, c, and d respectively. According to Figure 2.12a, a gross slip condition exists at the beginning of the experiment. However, a partial slip condition exists after 500 cycles (Figure 2.12b). Thus, the gross slip condition turns into the partial slip condition before 500 hundred cycles. After these cycles, the frictional force reaches a nearly steady value until the crack is nucleated at the contact region. Therefore, the frictional force hysteresis loops remain nearly the same between 500 cycles and 20,000 cycles (Figure 2.12c). The frictional force carrying capacity reduces when the cyclic axial force is applied to the specimen in the direction of

tension due to crack formation. It is also possible to observe the reduction in the two dashed lines in the above figure. The crack closes under compression; therefore, the frictional force carrying capacity does not change in this direction. According to Figure 2.12d, frictional force carrying capacity declines in both pads. This result indicates that the crack nucleates on both sides of the specimen in the contact region unlike in test 1.

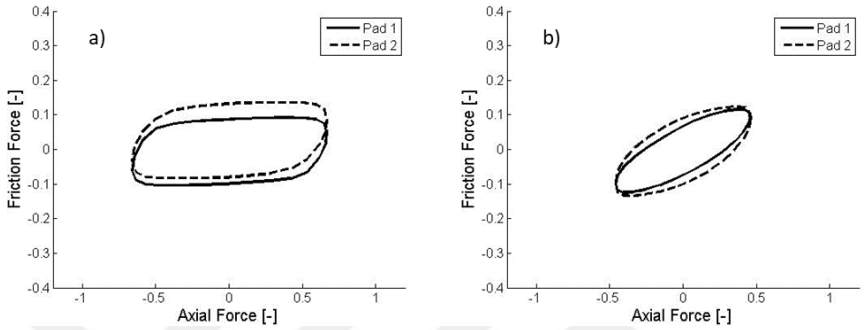


Figure 2.13. Frictional force vs. applied load hysteresis loop for (a) test 2 (Pad=15-5PH, R=-1, $\sigma_a = 1.82$, N=182,663 Cycles), (b) test 3 (Pad=15-5PH, R=-1, $\sigma_a = 1.27$, N=499,286 Cycles

To understand if the axial cyclic load has an effect on the contact condition in the first cycle, the hysteresis loops of test 2 and 3 are compared. The frictional force hysteresis loops during the first cycle of the experiment for test 2 and 3 can be seen in Figure 2.13. The applied bulk stress is 1.82 in Figure 2.13a and 1.27 in Figure 2.13b. The amount of axial cyclic stress changes the shape of the hysteresis loops as seen in the above figure so it can be concluded that axial cyclic stress has an important effect at the beginning of the test. At higher applied axial cyclic stress values, the test begins in the gross slip regime. On the other hand, if the applied axial cyclic stress value is small enough, then the test starts under partial slip condition. This result implies that the applied axial cyclic stress plays an essential role over the existing condition of the contact area.

### 2.2.3. Fretting Scars

To achieve more precise results, contact regions should be examined. Although stick and slip regions have been experimentally investigated, the visuals of the specimen can also provide fruitful explanations. As such, the contact surfaces where the primary and small cracks exist are investigated. The contact area, applied cyclic axial loading direction and primary cracks can be seen in the following figures.

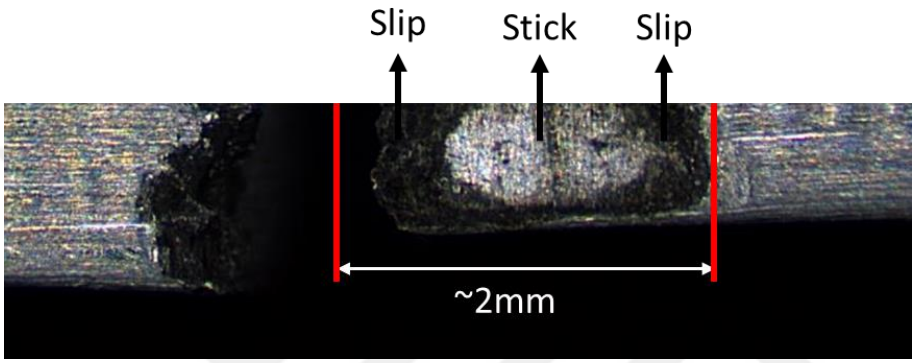


Figure 2.14. Fretting scars on the contact region of test 1

The contact region which includes primary cracks resulting from the steel-aluminum contact case is depicted in Figure 2.14. The normalized applied cyclic stress is 2.72. The thickness of the pad feet is 2mm. It is observed that the contact width is less than 2 mm because the experiments are performed with a cylindrical on flat contact configuration. Since the pad is of a cylindrical shape, only a part of the pad can be in contact with the specimen. This leads to smaller contact area when it is compared to a flat-on-flat contact configuration. According to Figure 2.14, stick-slip regions exist in the contact area. The slip regions are located at both the leading and trailing edges of the contact area. However, a stick region exists only at the center of the contact area.

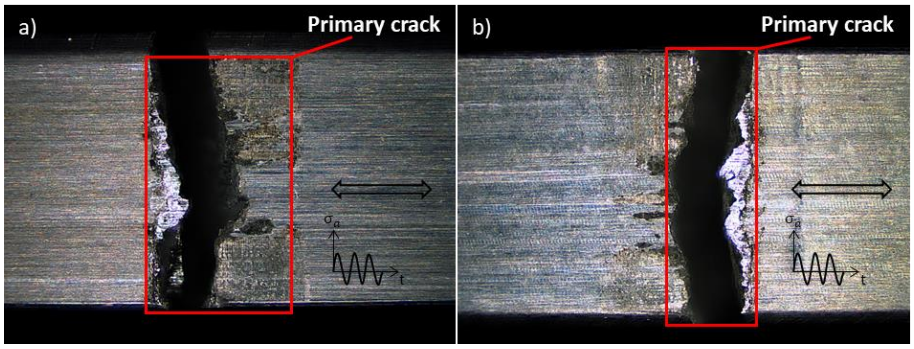


Figure 2.15. Primary cracks on the contact regions for test 9 (Pad= AL7050 T7451, R=-1, $\sigma_a$ =2.72) (a) left side of the specimen (b) right side of the specimen

The contact region resulting from the aluminum-aluminum contact case is shown in Figure 2.15. The stick and slip regions are found on the contact surface. It is observed that the slip region only exists at the trailing edge of the contact area. The entire area outside this slip region appears to be stick condition. On the other hand, slip regions are observed both in the leading and trailing edges of the contact region for the steel-aluminum contact case under the same loading conditions. This result indicates there exists a bending in the fretting pad feet. The bending in the pad feet is higher for the tests performed with an aluminum pad. The results suggest that this bending could be eliminated using stiffer pad material.

Two primary cracks are observed on the specimen surfaces. These cracks nucleated at both sides of the specimen. The observed primary cracks can be seen in Figure 2.15a and Figure 2.15b. Usually, it is expected that the main crack due to fretting fatigue will be nucleated at the stick/slip boundary or nearly at the end of the contact region [60]. Still, there is no exact point for the crack initiation location. In this test cracks are initiated close to the end of the contact area.

As well as primary cracks, fretting scars were observed after the experimentation phase. The fretting scars on the contact surface are shown in Figure 2.16 and Figure 2.17. The stick and slip regions can be seen on the contact regions. The dark areas represent the slip regions.

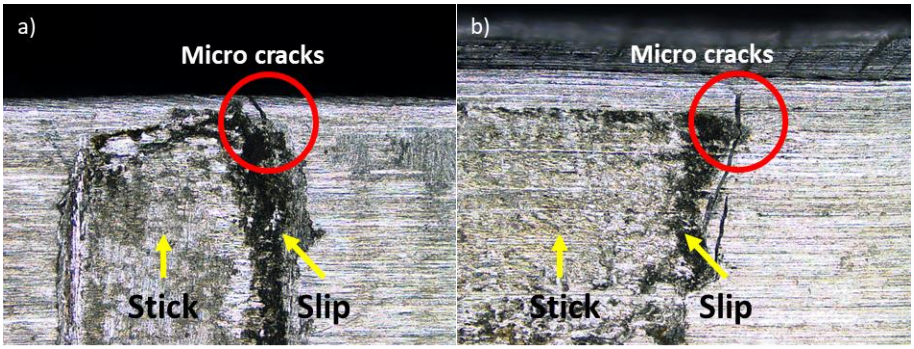


Figure 2.16. Fretting scars on the contact region (a) test 1 (Pad=15-5PH, R=-1, $\sigma_a$=2.72), (b) test 4 (Pad=15-5PH, R=-1, $\sigma_a$=1.00)

The effect of the axial cyclic loading on the contact region in terms of the resulting fretting scars are examined in Figure 2.16. The applied cyclic axial stress is $\sigma_a = 2.72$ for test 1 (Figure 2.16a) and $\sigma_a = 1.00$ for test 4 (Figure 2.16b). The same pad material was used in both tests to highlight the effects of axial cyclic stress. It can be observed that the slip area for test 1 is darker than test 4. Dark regions occur due to surface wear during the experiment. This observation indicates that the slip amplitude on the contact region is highly dependent on the magnitude of the cyclic axial loading.

In addition, micro cracks can be observed in the contact regions which are noted by red circles in Figure 2.16. These cracks are also known as non-propagating cracks. In the contact region, there are many small cracks (i.e. non-propagating cracks), in addition to the primary crack. Micro cracks are located in the slip region for test 1 and at the end of the contact area for test 4.

Although, it is expected that cracks initiate at both side of the specimen during the experiment, the results shows that usually, a primary crack initiates on one side of the specimen.

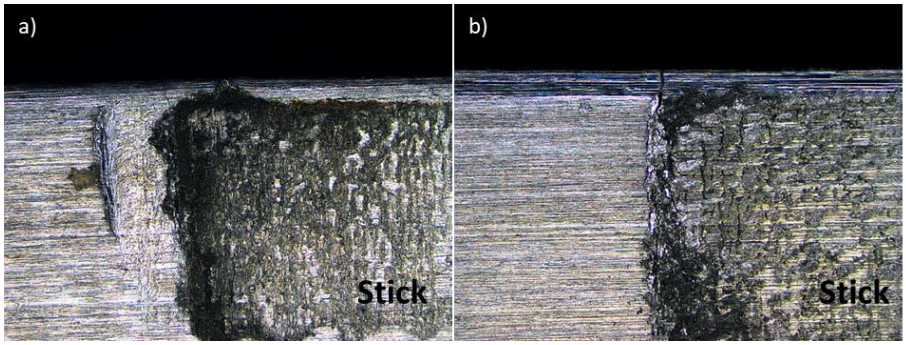


Figure 2.17. Fretting scars in the contact region (a) test 1 (Pad=15-5PH, R=-1, $\sigma_a$=2.72), (b) test 9 (Pad= AL7050 T7451, R=-1, $\sigma_a$=2.72)

The pad material effects on the stick region are shown in Figure 2.17. Both tests were performed under the same loading conditions. The pad material is 15-5PH steel in test 1 (Figure 2.17a) and AL7050 T7451 in test 9 (Figure 2.17b). It can be observed that the colors on the stick regions are different in both experiments. This result could be explained by the bedding in process or micro-slip in the stick region. It also can be observed that the relative slip amplitude value for the same loading conditions with different pad materials is higher for the condition of steel-aluminum contact. In both cases, these findings indicate that aluminum-aluminum contact has a higher friction coefficient when compared to the condition of steel-aluminum contact case; since the dark color represents wear, and the stick region for the steel pad is darker than the aluminum pad. These results are also verified with the friction force variation curve provided in Figure 2.9.

### 2.2.4. Fretting Cracks

In this section, primary crack faces are examined for the failed fretting AL7050 T7451 aluminum specimens. The changes in the crack faces due to pad material and axial cyclic stress value are examined. The crack formation locations are investigated for test 1, test 3, test 6 and test 10.

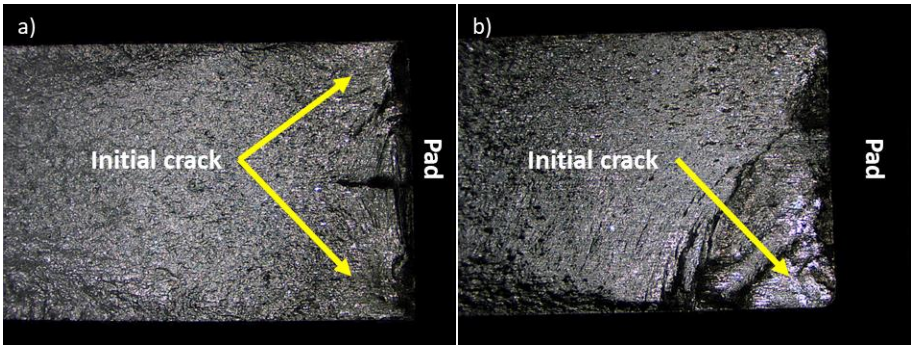


Figure 2.18. Crack surfaces on specimens (a) test 1 (Pad=15-5PH, R=-1, $\sigma_a$=2.72), (b) test 3 (Pad=15-5PH, R=-1, $\sigma_a = 1.27$)

To shed light on crack propagation behavior of the specimen, the fretting fatigue test results are compared in terms of the crack face. The crack face of fretting specimens for test 1 and test 3 are given in Figure 2.18. In both experiments 15-5PH steel pads were used. Test 1 was performed with a low cycle fatigue regime and test 3 was performed with a high cycle fatigue regime. The specimen was subjected to a higher axial cyclic loading in test 1 than in test 3. The main crack nucleated at the edges of the specimen in test 1 and at only one of the edges of the specimen in test 3. The crack nucleation locations can be seen in Figure 2.18.

The effect of the fretting conditions on the crack face is weak in terms of crack propagation in test 1. After the crack nucleation process, it is observed that the crack propagates due to cyclic axial loading (Figure 2.18a). On the other hand, the stresses that occur due to fretting conditions have an important effect on the crack propagation in test 3 (Figure 2.18b). According to comparison in terms of crack behavior, the fretting phenomenon has a powerful effect on the crack propagation in the first few millimeters in the high cycle fatigue regime.

In Figure 2.19, crack faces of the failed specimens are also compared between test 6 and test 10. AL7050 T7451 aluminum pads are used in both experiments, which were performed in high cycle regime. Specimens failed at 295,518 cycles in test 6 (Figure 2.19a) and at 220,223 cycles in test 10 (Figure 2.19b). According to Figure 2.19, the

primary cracks initiate at the edges of the specimens. Similar crack propagation behavior can be observed in both experiments.

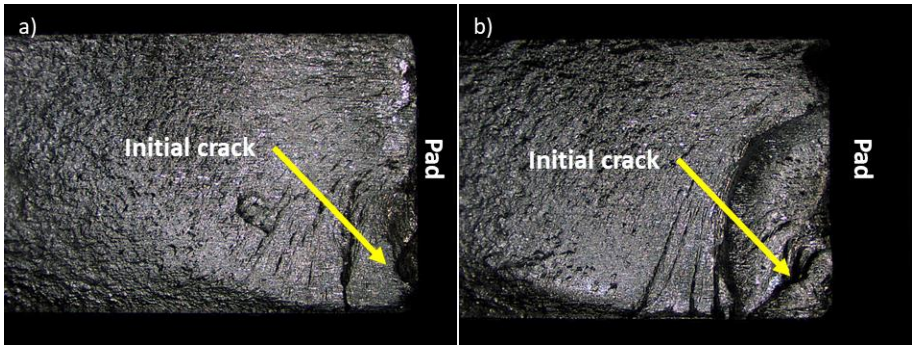


Figure 2.19. Crack faces on specimens (a) test 6 (Pad= AL7050 T7451, R=-1, $\sigma_a$=1.81), (b) test 10 (Pad= AL7050 T7451, R=-1, $\sigma_a$=2)

# CHAPTER 3

# FINITE ELEMENT ANALYSIS OF FRETTING FATIGUE CYCLE

In this chapter, fretting fatigue simulations are performed with finite element analysis. The finite element model is constructed in ABAQUS. Due to high experimentation costs and time, finite element simulations have crucial meaning for industrial applications. Thus, results from finite element analysis are compared with results from fretting fatigue experiments to justify simulations.

## 3.1. Theoretical Background

The Hertz Contact Theory and Mindlin Theory are explained in this section. This theory enables us to calculate the normal pressure on the contact region. The Hertz Contact Theory is also necessary to verify the finite element model. The Hertz Contact Theory is based on two contacted cylinders using a normal force (F). The aim of this theory is to obtain the pressure which occurs due to the contact of these cylinders. Two-dimensional plane strain conditions are valid away from the cylinder ends. In order to achieve the cylinder and half plane contact configuration, which is given in Figure 3.1, one of the radii of the cylinders is assumed as infinite.

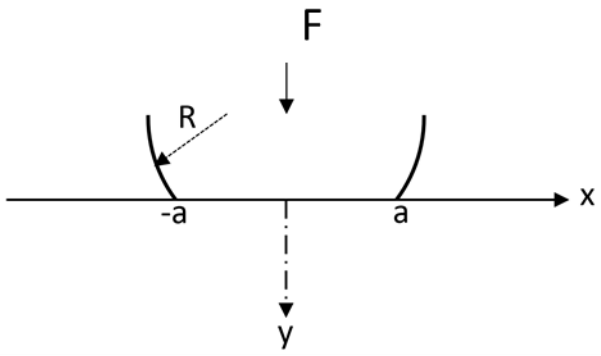


Figure 3.1. Hertz contact configuration with the half-space assumption

The Hertz Contact Theory [61] is capable of calculating the contact pressure in the case of different geometries or material properties of the contacting bodies without friction. A representative view of Hertz Contact as per Hertz Contact Theory is given in Figure 3.2.

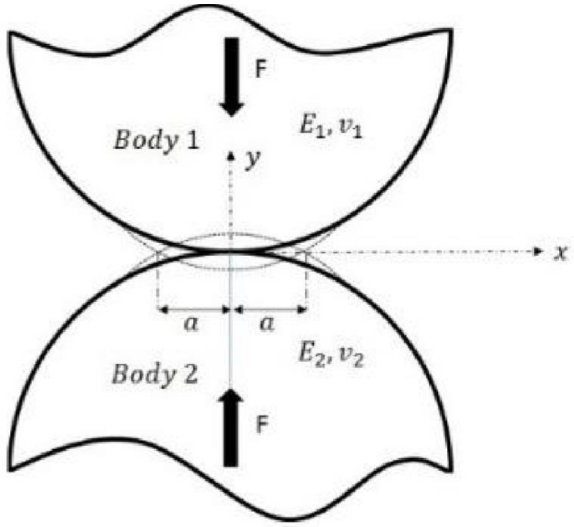


Figure 3.2. Representative view of Hertz Contact

According to the Hertz Contact Theory, when the contact conditions are achieved between the cylindrical bodies, a rectangular contact area takes place. This contact pressure is at its maximum at the center of the contact region and becomes zero at the edges of contact. The normal pressure distribution cannot be affected by any shear tractions. The calculation of the effective radius of curvature is given as,

$$k = \frac{1}{R_1} + \frac{1}{R_2}. \tag{3.1}$$

Bodies may have different material properties from each other. Thus, the effective modulus of elasticity (compliance) should be calculated with (3.2).

$$A = 2\left(\frac{1 - v_1^2}{E_1} + \frac{1 - v_2^2}{E_2}\right). \tag{3.2}$$

Pressure distribution in the contact area can be calculated as,

$$p(x) = -\frac{2F}{\pi a l}\sqrt{1-\left(\frac{x}{a}\right)^2}. \tag{3.3}$$

The maximum pressure is found at the center of the contact region where x is zero. The maximum pressure is calculated as,

$$P_0 = \frac{2F}{\pi a l}. \tag{3.4}$$

To obtain the half width of the total contact area the following equation should be used.

$$a = \sqrt{\frac{2FA}{\pi k l}}. \tag{3.5}$$

where $E_i$, $v_i$ , $R_i$ are the elastic modulus, Poisson's ratio and radius of the top and bottom surfaces for i=1,2, respectively and $l$ is the thickness of the contact area.

Mindlin and Dereiswicz [62] further developed the Hertz theory to include the effect of the tangential load which takes into account the effect of friction coefficient. They divided the contact region into two regions consisting of stick and slip regions which can be seen in Figure 3.3.

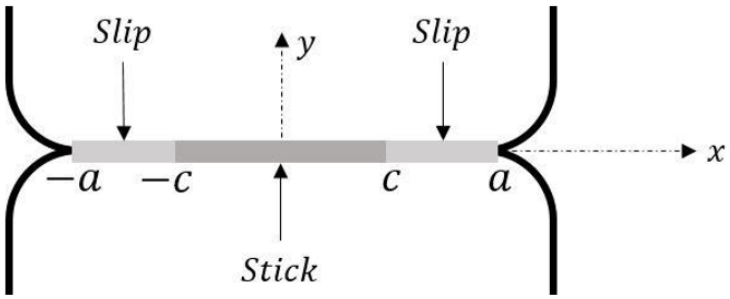


Figure 3.3. Representative view of the stick and slip region

According to Mindlin theory, the normal pressure distribution remains unchanged whereas shear tractions are developed to sustain the tangential force. The shear traction distribution $q(x)$, is calculated as

$$q(x) = \begin{cases} -fP_0\sqrt{1-\left(\frac{x}{a}\right)^2} & c \le |x| \le a \\ -fP_0\left[\sqrt{1-\left(\frac{x}{a}\right)^2} - 2\frac{c}{a}\sqrt{1-\left(\frac{x}{c}\right)^2}\right] & |x| < c \end{cases} \quad (3.6)$$

where $f$ is the friction coefficient and $c$ is the length of the stick region. The ratio of the stick region to the total contact area can be calculated as,

$$\frac{c}{a} = \sqrt{1-\frac{Q}{fF}}. \quad (3.7)$$

where $Q$ is the tangential force.

However, Hills and Nowell (1993) showed that when the shear loading is generated by an axial bulk stress applied to one component, the stick region is shifted by the eccentricity value e which causes a change in the shear traction distribution given by the following equation,

$$q(x) = \begin{cases} -fP_0\sqrt{1-\left(\frac{x}{a}\right)^2} & c \le |x| \le a \\ -fP_0\left[\sqrt{1-\left(\frac{x}{a}\right)^2} - 2\frac{c}{a}\sqrt{1-\left(\frac{x+e}{c}\right)^2}\right] & |x+e| < c \end{cases} \quad (3.8)$$

where eccentricity, $e$, can be calculated as,

$$e = \frac{a\sigma_{axial}}{4\mu P_0}. \quad (3.9)$$

### 3.2. Fatigue Methodology

Total fretting fatigue life of fretting specimen consists of the initiation life and propagation life. In this work, initiation and propagation life models are used separately to calculate a combined total fatigue life.

#### 3.2.1. Initiation Life

Under fretting fatigue condition, a complex stress field is expected due to both cyclic axial stress and normal pressure exerted on the contact region. Thus, a multiaxial fatigue criterion is required for an accurate prediction of the crack initiation life, $N_i$. Although there are many other approaches for multiaxial fatigue, critical plane approaches have been widely used in the literature for fretting fatigue which is also followed here. The advantage of a critical plane model is that it not only can predict the fatigue life, but also can estimate the orientation of the crack. Critical plane approaches employ stress, strain or energy quantities to calculate the damage on the surface.

In this study, Fatemi-Socie critical plane criterion [63] is utilized. To clarify the stress field on the substrate material under fretting conditions, representative stress state is given for a point in Figure 3.4.

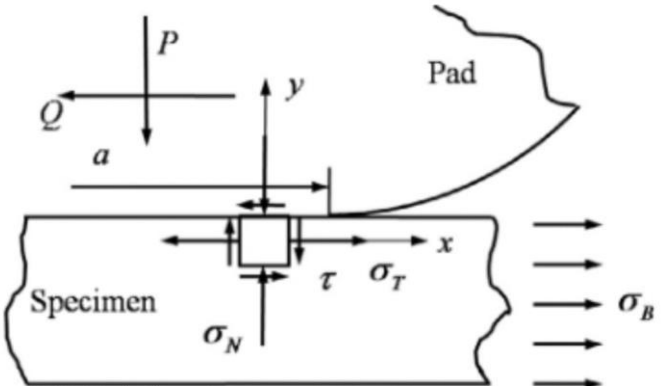


Figure 3.4. The stress state of a point in the contact interface of a specimen [64]

The normal stress and shear strains on a plane oriented at $\theta$ is calculated using stress and strain transformation equations by changing theta, $\theta$, from $-90^o$ to $90^o$. These stress and strain transformations are performed for each node on the specimen surface as shown in Figure 3.5.

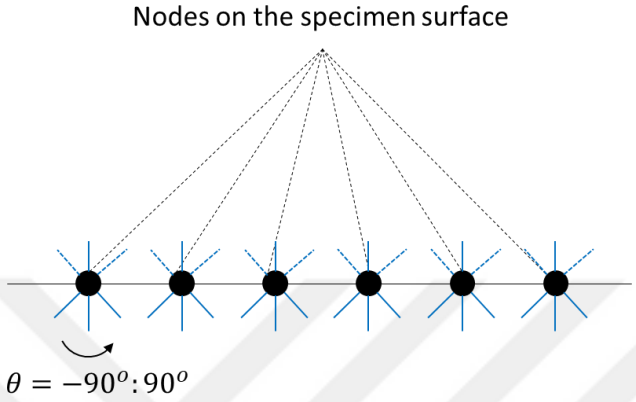


Figure 3.5. Representative view of the nodes on the specimen surface

The stress-strain transformation equations are defined as,

$$\sigma_\theta = \frac{\sigma_x + \sigma_y}{2} + \frac{\sigma_x - \sigma_y}{2} cos2\theta - \tau_{xy} sin2\theta, \tag{3.10}$$

$$\frac{\gamma_\theta}{2} = -\frac{\varepsilon_x - \varepsilon_y}{2} sin2\theta - \frac{\gamma_{xy}}{2} cos2\theta. \tag{3.11}$$

The Fatemi-Socie critical plane model is based on the range of shear strain $\Delta\gamma_{max}$ in the critical plane. The Fatemi-Socie damage parameter is defined as

$$FS = \frac{\Delta\gamma_{max}}{2}\left(1 + k\frac{\sigma_{n,max}}{\sigma_y}\right), \tag{3.12}$$

where $\sigma_{n,max}$ is the normal stress exerted on the critical plane, $\sigma_y$ is the yield strength and $k$ is a constant that is usually determined from fatigue tests [65]. The constant can be defined as,

$$k = \frac{\sigma_y}{\sigma'_f}, \tag{3.13}$$

where $\sigma'_f$ is the fatigue strength coefficient found from representative S-N curves. Basquin constructed a relation between the stress and life of the material, given by the Basquin equation as,

$$\frac{\Delta\sigma}{2} = \sigma'_f (2N_i)^b, \tag{3.14}$$

where $b$ is defined as the fatigue strength exponent. The Fatemi-Socie parameter (FS) can be simplified for the stress ratio, R = -1. The equation then becomes:

$$FS = \frac{1+v}{E}\sigma'_f (2N_i)^b \left(1 + \frac{1}{2}(2N_i)^b\right). \tag{3.15}$$

For the crack nucleation analysis, the normal stress and shear strain on each plane are calculated using equations (3.10) and (3.11). The damage on each plane is then calculated using these normal stress and strains. The highest damage parameter is used for crack initiation life calculations by using the Fatemi-Socie approach fatigue life equation (3.15). The flowchart showing the steps of the crack initiation life calculation is given in Figure 3.6. The crack initiation life flowchart requires FE analysis only for one full fatigue cycle. The MATLAB code required for analysis is given in Appendix C.

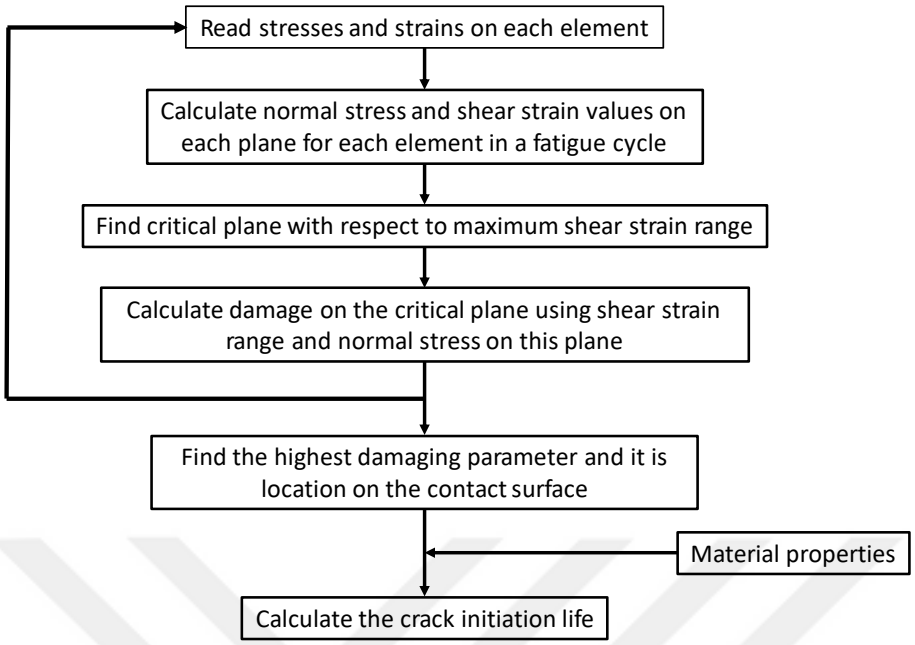


Figure 3.6. The crack initiation life calculation flowchart

### 3.2.2. Propagation Life

For the second phase, the crack propagation life is calculated. The initial crack location is obtained by the critical plane methodology from the previous section. The initial crack length is assumed to be 0.05 mm in size, which is slightly higher than or equal to the size of few grains of aluminum alloys as recommended in the literature [66, 67]. The crack propagation life ($N_p$), is calculated between the initial crack nucleation and crack growth to the critical crack length where total failure occurs. Crack propagation life is calculated by considering the fracture mechanics approach using the Paris Law. The crack growth rate against the range of stress intensity factor equation is given by,

$$\frac{da}{dN} = C\Delta K^m, \tag{3.16}$$

where $\Delta K$ is taken as,

$$\Delta K = K_{\mathrm{I},max}\,. \tag{3.17}$$

In Equation 3.13, $C$ and $m$ values are material properties and are taken from the NASGRO database for AL7050 T7451. The crack propagation life is obtained from the integration of Equation 3.13 when the stress intensity factor is known as a function of a/W (using two techniques explained in the following sections).

Even though fretting fatigue experiments are performed under the R=-1 loading condition, the da/dn curve for R=0 is used for the crack propagation life calculation. This is because the applied axial cyclic load in the compression direction has no effect on crack propagation [68]. Although there are mode I and mode II conditions at the crack tip, the mode I stress intensity factor is used for crack propagation life calculations since it is assumed that the crack will propagate perpendicular to the contact surface.

In order to obtain the stress intensity factor (SIF) values for Equation 3.13, weight function method and finite element method are utilized in this work. Detailed explanations of the weight function method and the Seam crack methodology are given in the subsections that follow.

#### 3.2.2.1. Weight Function Method

The weight function method uses the stress field obtained from the finite element model which does not contain any cracks, which means that the use of the finite element model is constructed for fretting contact. The contact situation between the crack faces is ignored in this method [39]. To calculate the crack propagation life, the stress intensity factor (SIF) should be obtained during each crack increment step used. Therefore, the weight function and the geometry of the crack body are two inter-related concepts. As long as the weight function is known, to calculate the stress intensity factor it is only necessary to know the stress field, which is the result of the load on the analyzed body. In this study, a single edge crack in a finite plate weight function is used. A representative fretting fatigue model with a crack is shown in Figure 3.7.

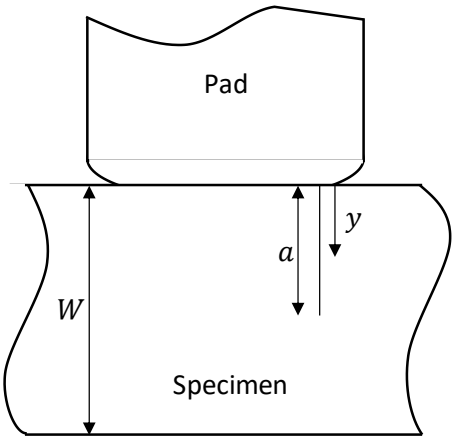


Figure 3.7. Representative crack on the specimen

The weight function equation is given as [69],

$$m(y,a) = \frac{2F}{\sqrt{2\pi(a-y)}}\left[1 + M_1\left(1-\frac{y}{a}\right)^{1/2} + M_2\left(1-\frac{y}{a}\right) + M_3\left(1-\frac{y}{a}\right)^{3/2}\right], \tag{3.18}$$

where W is the thickness of the specimen, a is the crack length and y is a variable that measures the distance to the crack tip. The parameters $M_1$, $M_2$ and $M_3$ are dependent on the crack configuration. For a single edge crack in a finite width plate, these parameters are given as [70],

$$M_1 = \frac{-0.029207 + \frac{a}{W}\left(0.213074 + \frac{a}{W}\left(-3.029553 + \frac{a}{W}\left(5.901933 - \frac{a}{W}2.657820\right)\right)\right)}{1.0 + \frac{a}{W}\left(-1.259723 + \frac{a}{W}\left(-0.048475 + \frac{a}{W}\left(0.481250 + \frac{a}{W}\left(-0.526796 + \frac{a}{W}0.345012\right)\right)\right)\right)} \tag{3.19}$$

$$M_2 = \frac{0.451116 + \frac{a}{W}\left(3.462425 + \frac{a}{W}\left(-1.078459 + \frac{a}{W}\left(3.558573 - \frac{a}{W}7.553533\right)\right)\right)}{1.0 + \frac{a}{W}\left(-1.496612 + \frac{a}{W}\left(0.764586 + \frac{a}{W}\left(-0.659316 + \frac{a}{W}\left(0.258506 + \frac{a}{W}0.114568\right)\right)\right)\right)} \tag{3.20}$$

$$M_3 = \frac{0.427195 + \frac{a}{W}\left(-3.730114 + \frac{a}{W}\left(16.276333 + \frac{a}{W}\left(-18799956 - \frac{a}{W}14.112118\right)\right)\right)}{1.0 + \frac{a}{W}\left(-1.129189 + \frac{a}{W}\left(0.033758 + \frac{a}{W}\left(0.192114 + \frac{a}{W}\left(-0.658242 + \frac{a}{W}0.554666\right)\right)\right)\right)} \tag{3.21}$$

The weight function equation is seen to be dependent on $a/W$. Using this weight function, the stress intensity factor can be obtained from the expression

$$K_{\mathrm{I}} = \int_0^a \sigma_x(y) m(y,a) dy, \tag{3.22}$$

where, $\sigma_x$ is the normal stress in the direction perpendicular to the crack plane. The flowchart showing the steps of the crack propagation life calculation is given in Figure 3.8. The MATLAB code for representative calculations is given in Appendix D.

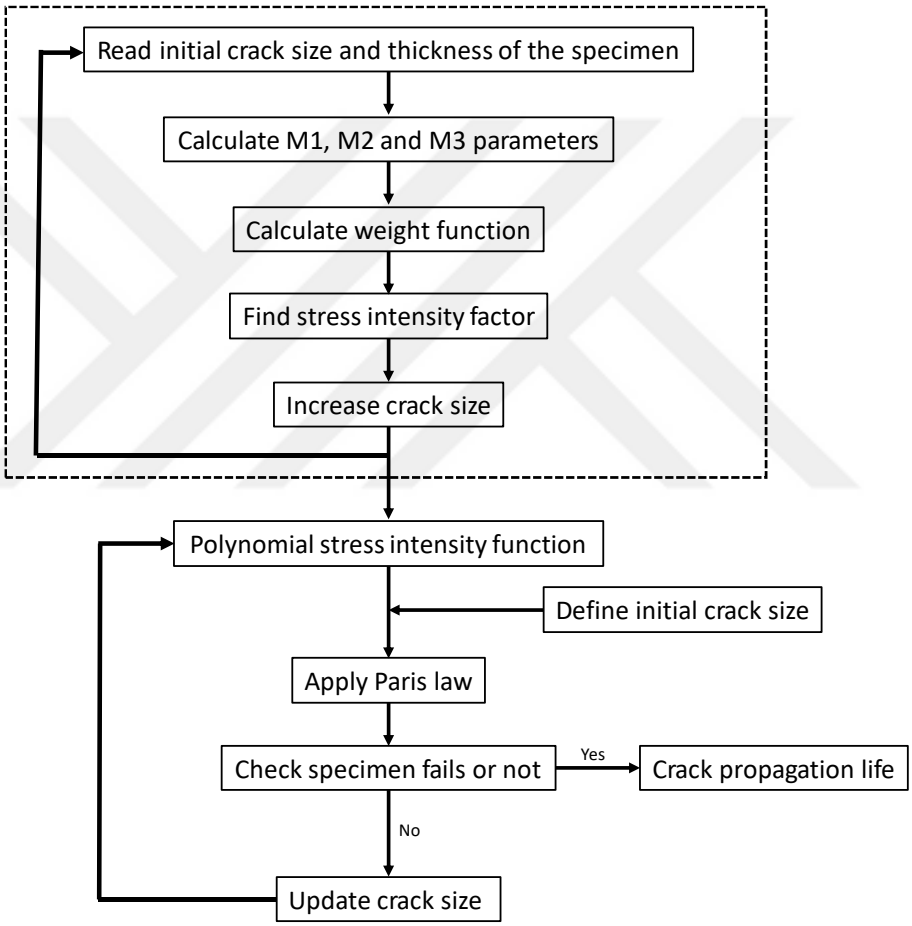


Figure 3.8. The crack propagation life calculation flowchart

### 3.2.2.2. Seam Crack Methodology

There are different types of crack creation methods in ABAQUS such as the slot type crack method, the seam crack method and the extended finite element method

(XFEM). In this study, seam crack methodology is utilized due to its better estimate in calculating the stress intensity factor around the crack tip. The slot type crack method cannot calculate a sufficiently accurate SIF. XFEM generally is not used in 2D models; it needs additional subroutines to extract SIF in 2D models.

In seam crack methodology, a line called a seam is used to define the crack in a body for two dimensional problems [71]. A seam embedded in a two-dimensional part is shown in Figure 3.9. In order to create this seam, the 2D surface should be partitioned to define the crack line.

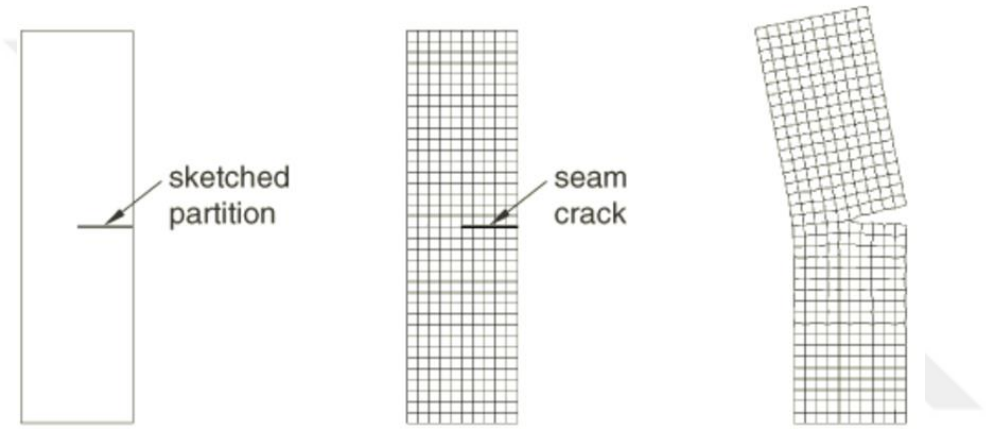


Figure 3.9. A seam embedded in a face [71]

ABAQUS creates independent duplicate nodes on this crack line to allow the crack faces to separate from each other. This method enables the defined crack to open or close depending on the loading conditions. The interaction of the crack faces at the closing mode of the crack is defined with a contact module. A zero friction coefficient is used, and the normal behavior and tangential interactions are not defined between the crack faces.

There is a high stress gradient at the crack tip. Thus, the mesh should be fine enough to capture this abrupt change in the stress distribution. In the literature, quarter-point elements and a radial quadratic mesh pattern are recommended to estimate the stress intensity factor accurately at the crack tip [72]. The quarter-point elements are created

by moving the mid-side nodes to the quarter edge of the elements as shown in Figure 3.10. Circular partitions are created around the crack tip to create radial transition elements as shown in Figure 3.11.

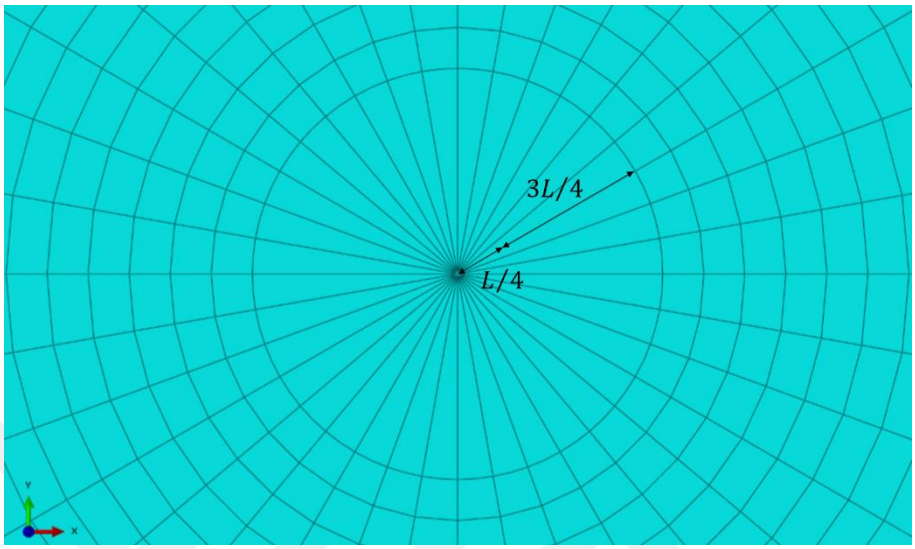


Figure 3.10. Circular mesh pattern around the crack tip

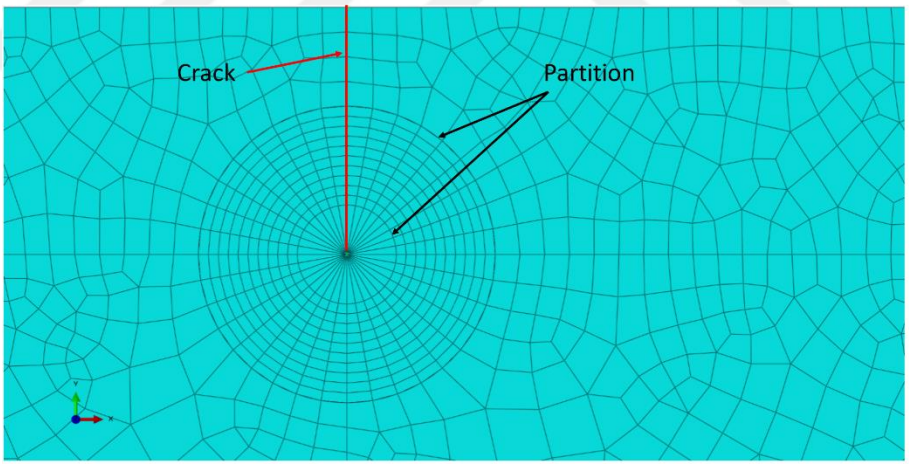


Figure 3.11. Circular partitions around the crack tip

Seam crack methodology uses a contour integral method to calculate the stress intensity value. Ten contour integrals are considered in the calculations. The representative contours around the crack tip are shown in Figure 3.12. The results of the first two contours are found to be erroneous so they are neglected [71]. Therefore,

the stress intensity factor is calculated by averaging the SIF values from the remaining 8 contours. The stress intensity value for a single edge crack in a finite plate is calculated using seam crack methodology, the weight function method and NASGRO software to validate the finite element model. The determined results are given in Appendix D. The study is performed to see the effect of the mesh size around the crack faces in terms of stress intensity factor. The results are given in Appendix E.

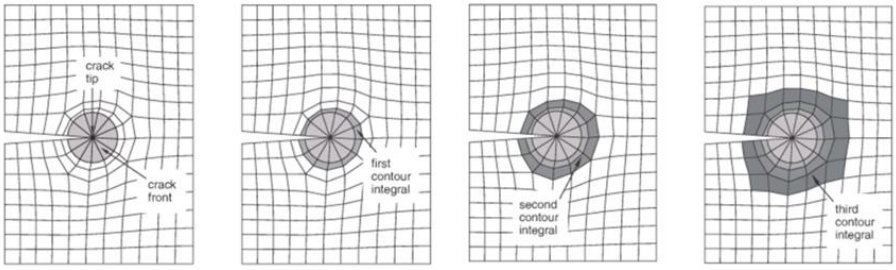


Figure 3.12. Representative contour integrals around the crack tip [71]

The maximum tangential stress criterion is utilized to determine the crack propagation direction. The representative view of the stresses at the crack tip is shown in Figure 3.13. The maximum tangential stress at the crack tip and the crack propagation angle has to be orthogonal. The near crack tip stress field for a homogeneous, isotropic linear elastic material is given by [73],

$$\sigma_{\theta\theta} = \frac{1}{\sqrt{2\pi r}} \cos\theta \left[ K_I cos^2 \frac{\theta}{2} - \frac{3}{2} K_{II} \sin\theta \right], \tag{3.23}$$

$$\tau_{r\theta} = \frac{1}{2\sqrt{2\pi r}} \cos\frac{\theta}{2} [K_{II} \sin\theta - K_{II}(3\cos\theta - 1)], \tag{3.24}$$

where, $r$ and $\theta$ are polar coordinates centered at the crack tip in a plane orthogonal to the crack face.

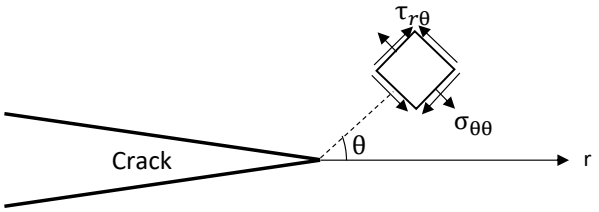


Figure 3.13. The representative view of the 2D stress state at the crack tip

The direction of crack propagation then can be obtained using either the condition

$$\frac{\partial \sigma_{\theta\theta}}{\partial \theta} = 0 \,, \tag{3.25}$$

$$\tau_{r\theta} = 0, \tag{3.26}$$

to obtain:

$$K_I \sin\theta_p + K_{II}\left(3\cos\theta_p - 1\right) = 0, \tag{3.27}$$

or

$$\theta_p = arccos\left[\frac{3K_{II}^2 + \sqrt{K_I^4 + 8K_I^2 K_{II}^2}}{K_I^2 + 9K_{II}^2}\right]. \tag{3.28}$$

The crack propagation angle $\theta_p$ is measured with respect to the crack plane.

### 3.2.3. Total Life

As it is stated before, the total fretting fatigue life of the substrate material is the sum of crack initiation and propagation lives. The total life $N_f$ can be calculated as,

$$N_f = N_i + N_p, \tag{3.29}$$

where, $N_i$ is the crack initiation life and $N_p$ is the crack propagation life, respectively.

## 3.3. Finite Element Model

The finite element model is constructed in order to obtain the stress field in the contact region without a crack. The cylinder on flat contact configuration is modeled to compare the results with experiments. The simulation of the fretting contact is achieved using ABAQUS™.

Half of the fretting pad and a quarter part of the specimen are modelled due to symmetry conditions. The bottom side of the quarter part of the specimen is constrained to the y-axis; and, to accomplish symmetry in x-axis, both the specimen and the pad are restricted in the x-direction. To simulate fretting contact conditions, axial cyclic loading is applied to the specimen and normal load is applied to the fretting

pad to create conditions similar to those in the experiments. The contact between the pad feet and the upper surface of the substrate material is achieved by applying a normal load at the top of the pad in the y-direction. The simulation has three main steps. In the first step, the normal load is applied and kept constant for the rest of the whole process. In the second step, to demonstrate the effect of the tangential loading in the contact region, the axial cyclic stress, which is distributed along the whole edge of the specimen, is applied to the right end of the specimen. In the final step, the same axial cyclic stress as in the second step is applied in the opposite direction. The loading locations and boundary conditions are shown in Figure 3.14.

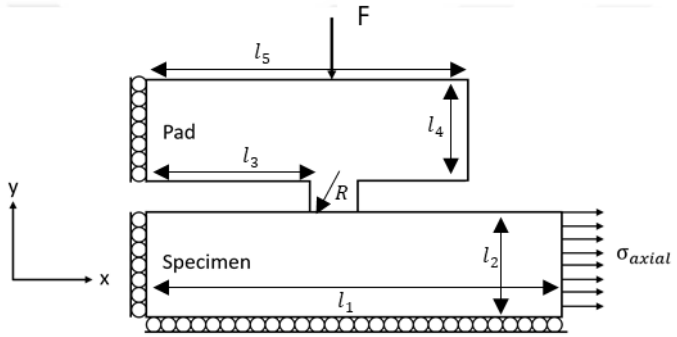


Figure 3.14. Loading locations and boundary conditions in the finite element model

where $l_1$= 25mm, $l_2$= 6,25 mm, $l_3$= 4 mm, $l_4$= 5 mm, $l_5$= 14 mm and $R$= 50mm.

The loading values, including the normal force and normalized cyclic axial stress values, are given in Table 3.1.

Table 3.1. Loading cases and normalized axial stress for the three steps

| | Step 1 | Step 2 | Step 3 |
|---|---|---|---|
| *F[N]* | 1500 | 1500 | 1500 |
| $\sigma_a$[-] | 0 | 1.82 | -1.82 |

A nonlinear, plane strain model [74-77] is utilized and a 2D quadrilateral, 4-node, plane strain, reduced integration element (CPE4R) is used in the model. The mesh size

area at the contact region is chosen as 5µm by 5µm. The mesh convergence study was performed for a similar fretting fatigue test setup [78]. The finite element model is shown in Figure 3.15.

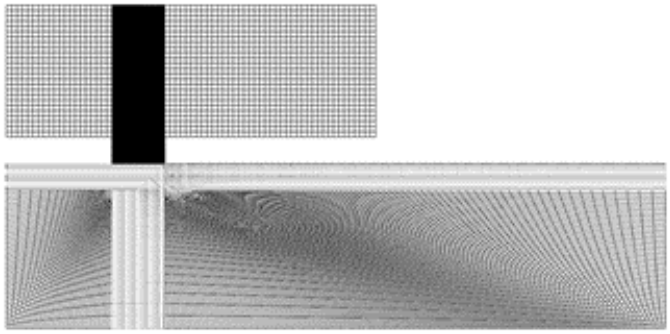

Figure 3.15. Finite element model of the fretting fatigue problem

A close-up view of the mesh around the contact region is shown in Figure 3.16.

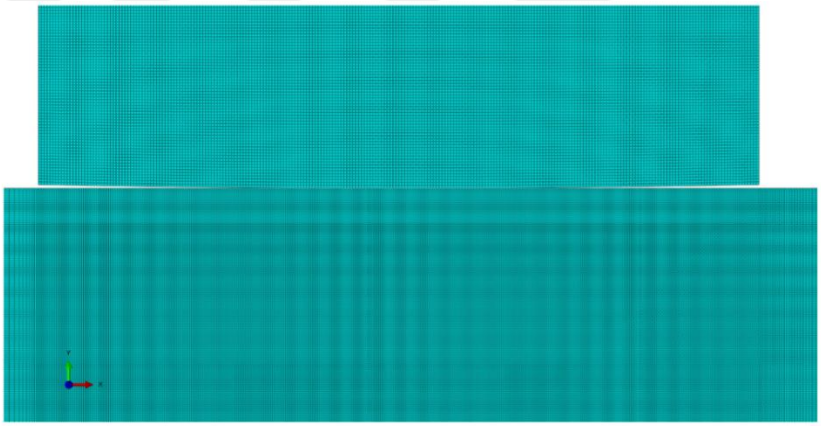

Figure 3.16. Mesh around the contact region

The contact between the pad feet and the upper surface of the specimen is achieved by using a master slave algorithm in ABAQUS [71]. A Lagrange multiplier formulation and an augmented Langrage algorithm are used for tangential behavior and normal behavior of the contact to simulate the Coulomb friction model respectively. Since the applied load leads to a rotation of the pad, Multi- Point-Constraint (MPC) is used to stabilize it. The master node of the MPC is selected as

the normal load application point and the slave part is chosen as the top surface of the fretting pad.

A second finite element model is created with a crack defined with the Seam crack methodology. The initial crack location is determined by using the Fatemi-Socie damage parameter from the uncracked finite element model. CPE8R and CPE4R elements are used for the crack tip and other locations, respectively.

The stress intensity factor calculation is achieved by the contour integral method. The mentioned model can be seen in Figure 3.17.

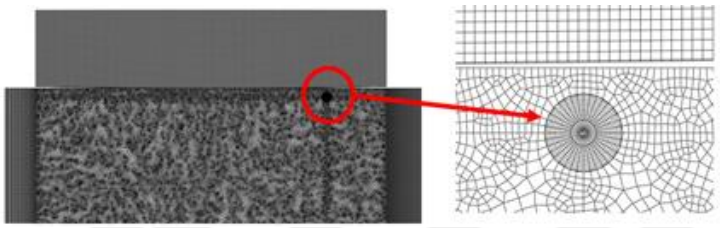

Figure 3.17. Finite element model of the initial crack of the fretting fatigue problem

### 3.4. Results

The results for the fretting fatigue lives for similar and dissimilar mating surfaces are presented herein. Stress and strain fields are obtained using finite element simulations which are used in calculating fatigue life estimates. For the model validation, the normal pressure at the contact surface obtained from finite element model is compared with the Hertz Contact Theory.

The crack initiation life and crack nucleation location for aluminum-aluminum and steel-aluminum are compared under the same normal load for different axial cyclic loads. Stress intensity factors and crack propagation lives are calculated using the respective finite element model and weight function method. Finally, a comparison between lives observed from experiments and calculated lives are provided.

### 3.4.1. Mesh Convergence Study

A mesh convergence study is performed for mesh sizes of 5, 10, 15 and 20 μm. The aluminum-aluminum contact condition is considered in the mesh convergence study. The normalized tangential stress distribution is used in the simulations. The tangential stress is normalized with applied axial stress. The applied normalized axial stress is 1.82. The normalized tangential stress distribution on the contact surface of fretted specimen is given in Figure 3.18. The results show that the tangential stress distribution is nearly similar for all mesh sizes. The tangential stress value reaches its maximum at the end of the contact area in the applied axial stress direction. Different stress results are observed at the peak point of the tangential stress distribution. To capture the peak stress at the end of the contact, the mesh size is selected as 5μm.

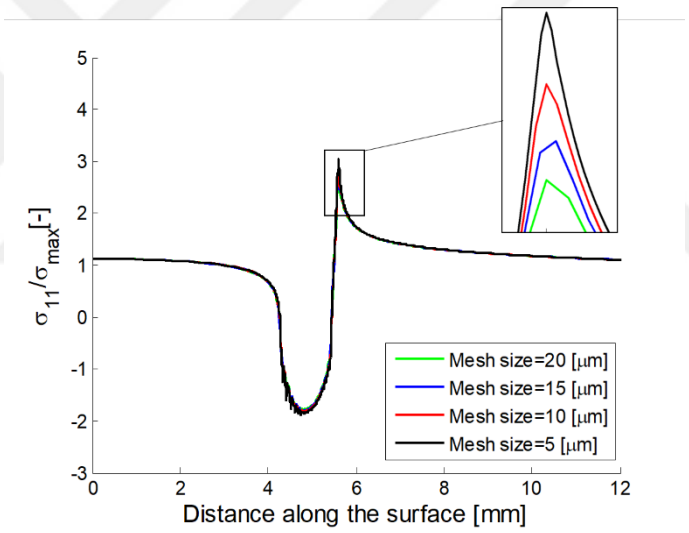


Figure 3.18. Maximum normalized tangential stress distribution on the contact surface of the specimen ($\sigma_a = 1.82$)

### 3.4.2. Model Validation

The cylindrical on flat contact configuration is achieved with the Hertzian Contact theory in simulations. The calculated normalized contact pressure distribution on the normalized contact area in simulations and the analytical results for both aluminum-aluminum contact and steel-aluminum contact cases are given in Figure 3.19. The x-

axis represents the contact surface of the specimen and the y-axis shows the normalized contact pressure. The pressure distribution reaches zero at the end of the contact area and it realizes its maximum value at the center of the contact area. It can be observed that the contact area is dependent on the pad material. When the pad material becomes softer, contact area increases. In addition, the change in the contact area affects the maximum value of the normal pressure. In other words, using stiffer pads in the contact area leads to an increase in the maximum value of the normal pressure.

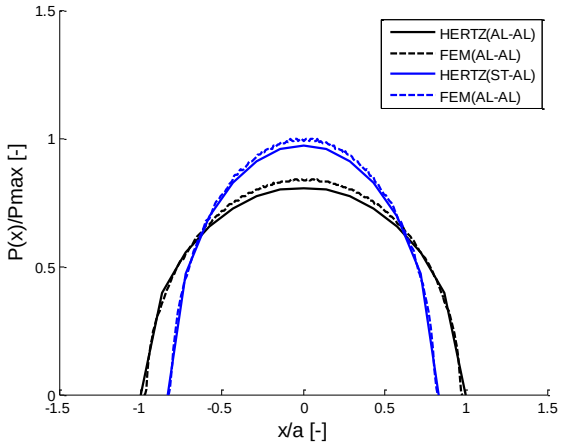


Figure 3.19. Pressure distribution in the contact area ($\sigma_a = 1.82$)

It is stated that Mindlin Theory is not an appropriate theory for shear traction distribution calculation when dissimilar materials are in contact. [74]

### 3.4.3. Crack Initiation Results

In this section, the crack nucleation point, and crack initiation lives are presented. The von Mises stress distribution is given in Figure 3.20. It is observed that stress distribution around the contact area for the steel-aluminum contact condition is higher than the aluminum-aluminum contact condition.

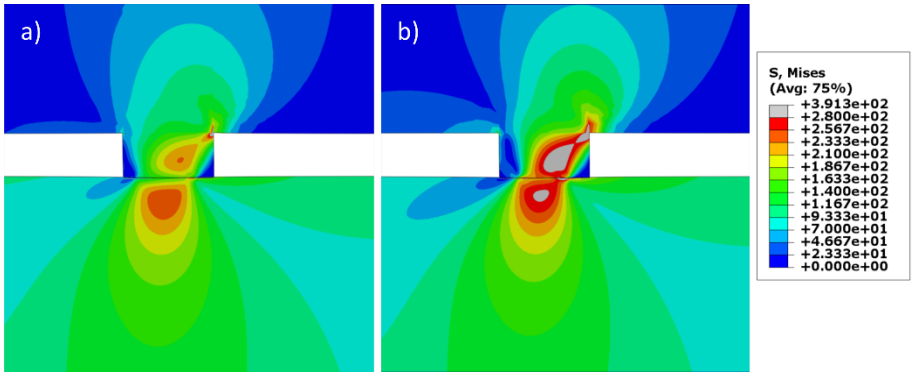


Figure 3.20. The von Mises stress distribution around the contact area (a) aluminum-aluminum contact, (b) steel-aluminum contact

The crack initiation life is calculated using the Fatemi-Socie critical plane approach. This approach is applied on the uncracked finite element model. The crack nucleation location on the contact area is also determined by calculating the Fatemi-Socie (FS) damage parameter. The damage maps for the aluminum-aluminum contact and steel-aluminum contact conditions are given in Figure 3.21 and Figure 3.22 respectively. The x-axis shows the specimen surface and the y-axis represents the F-S damage parameter. The crack nucleation location is expected at the peak location of the damage curve. It is observed that the crack nucleation location looks similar under different applied axial stress conditions for each case. In Figure 3.21, the area between two peaks at the leading and trailing edges approximates the stick region. The two peaks become closer when the applied axial cyclic stress increases. Since the areas between the two peaks decrease, it can be concluded that the stick region is dependent on the applied cyclic axial stress. The maximum F-S damage parameter value occurs near the stick-slip region and it is close to the trailing edge of the contact area. F-S damage parameter values increases with increasing applied axial cyclic loading. In Figure 3.22, a single peak is observed for each of the F-S damage parameter curves. Thus, the slip region is only expected at the trailing edge of the contact area for the aluminum-aluminum contact case. This result is also validated with the finite element results. When Figure 3.21 and Figure 3.22 are compared, a higher maximum F-S damage parameter is observed for the steel-aluminum contact case under the same

loading conditions when compared to the aluminum-aluminum contact case. Thus, lower crack initiation life is expected for a stiff pad.

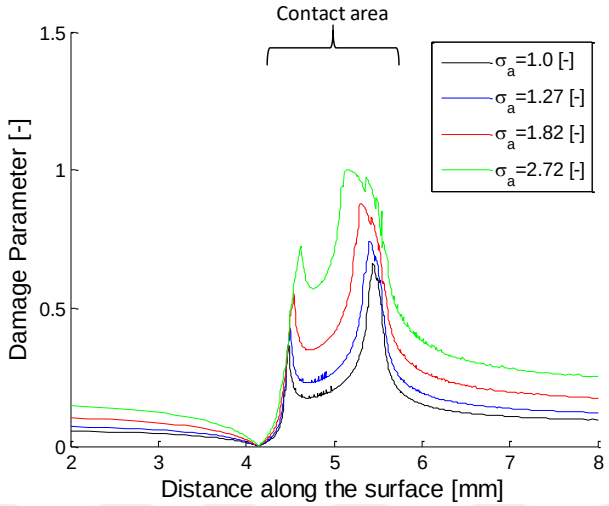


Figure 3.21. FS Damage parameter results for the steel-aluminum contact condition

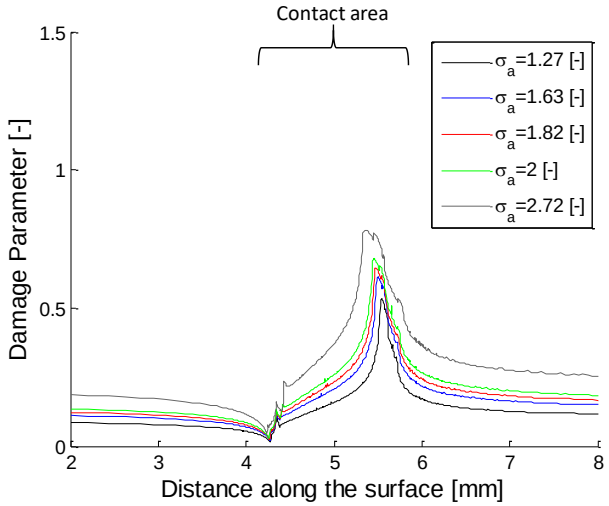


Figure 3.22. FS Damage parameter results for the aluminum-aluminum contact condition

### 3.4.4. Crack Propagation Results

In order to calculate the total fatigue life of the specimen crack propagation lives are calculated with the weight function method. The initial crack location is selected according to F-S damage parameter results. A single edge crack on a finite plate weight function method is considered when calculating the stress intensity values for each increment of the crack. Weight function results are also compared with the finite element simulation, which is performed with Seam crack methodology, in terms of both the stress intensity factor and crack propagation life results. The crack propagation directions for both the cases are shown in Figure 3.23 and Figure 3.24. According to the figure, the crack path is different for the first few crack increments. The crack propagates perpendicular to the contact surface. The reason is that the applied axial cyclic stress dominates crack propagation away from the contact surface.

Similar crack propagation directions are observed from the failed specimens (steel-aluminum contact) as shown in Figure 3.25. It is observed that the crack propagates nearly perpendicular to the contact surface after a few millimeters. This result indicates that the applied cyclic axial stress dominates the crack propagation path at the regions away from the fretted area.

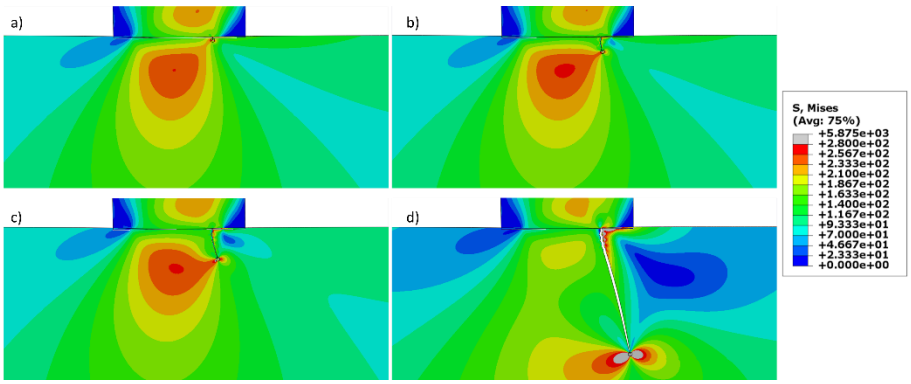


Figure 3.23. Crack length (a) 0.05 mm, (b) 0.25 mm, (c) 0.5 mm, (d) 2 mm for aluminum-aluminum contact ($\sigma_a = 1.82$), (b) steel-aluminum contact ($\sigma_a = 1.82$)

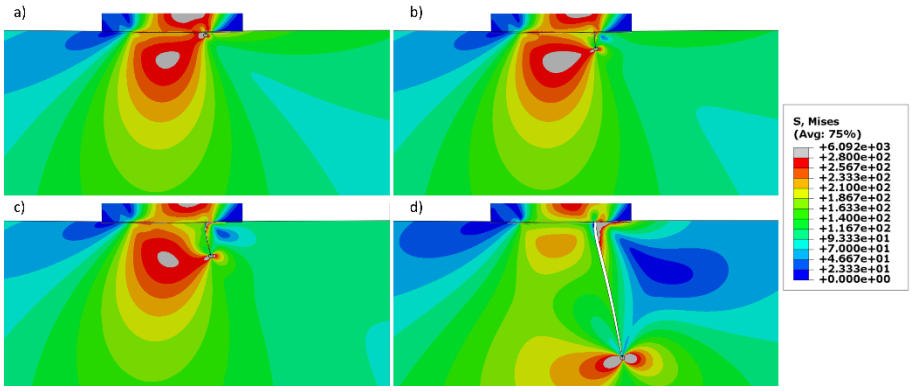


Figure 3.24. Crack length (a) 0.05 mm, (b) 0.25 mm, (c) 0.5 mm, (d) 2 mm for steel-aluminum contact ($\sigma_a = 1.82$)

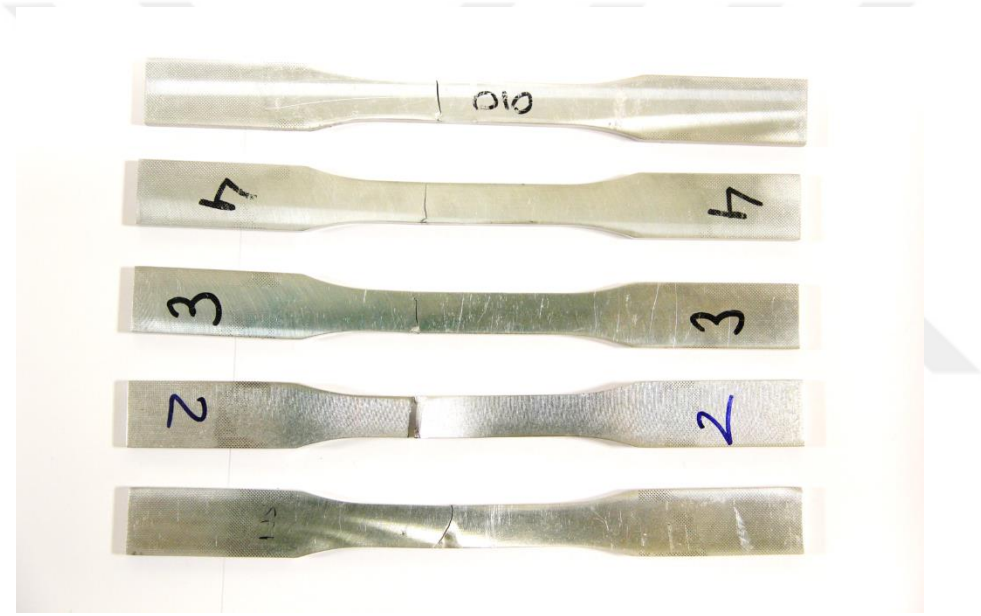

Figure 3.25. Specimens that have failed due to fretting fatigue (steel-aluminum contact)

The stress intensity factor results for the aluminum-aluminum contact and steel-aluminum contact cases are given in Figure 3.26 and Figure 3.27, respectively. The applied normalized cyclic axial stress is 1.82 in both cases. The x-axis represents the crack length and the y-axis shows the normalized stress intensity values during the crack propagation. The stress intensity factor results are compared for the first millimeter of the crack.

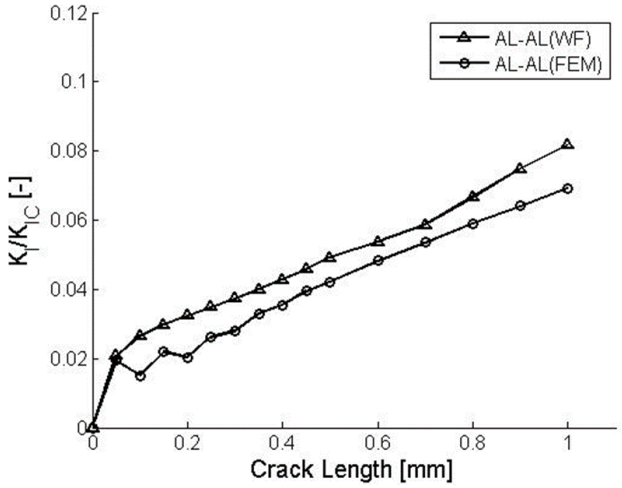


Figure 3.26. Stress intensity factor values during the crack propagation (Pad=Aluminum, $N_{exp}$=295,518 cycles)

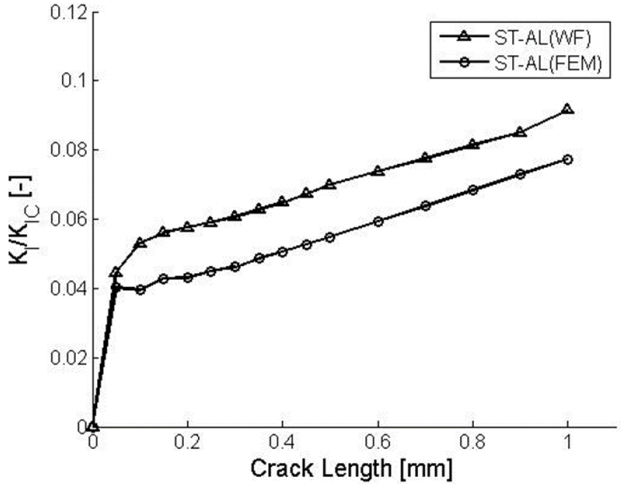


Figure 3.27. Stress intensity factor values during the crack propagation (Pad=Steel, $N_{exp}$= 182,663 cycles)

In Figure 3.26 and Figure 3.27, it can be observed that the stress intensity factor calculated from the weight function method and the finite element simulations give similar results. The differences between the results originate from the crack propagation direction. It is assumed that the initial crack is perpendicular to the contact surface in both cases. However, the weight function method assumes that the crack always propagates perpendicular to the surface. The crack propagation direction is

obtained via the Maximum Tangential Stress Criterion for the Seam crack methodology. Thus, the crack could change its direction during the propagation step during the simulation. Upon examination it is observed that the stress intensity factors obtained from the weight function method produce slightly higher results than those obtained from the contour integral method with ABAQUS. The stress intensity factor results obtained from both the finite element simulations and the weight function method indicates that the SIF values for the steel-aluminum contact condition are higher than those for the aluminum-aluminum contact condition under the same loading conditions. To calculate the crack propagation lives for each specimen with the SIF values obtained from each crack increment, a polynomial equation is defined for each loading case. These equations are employed via a linear fracture mechanics approach. The propagation lives up until the crack reaches 2 mm for the steel-aluminum contact and aluminum-aluminum contact conditions for both the weight function method and the finite element simulations, are shown in Figure 3.28.

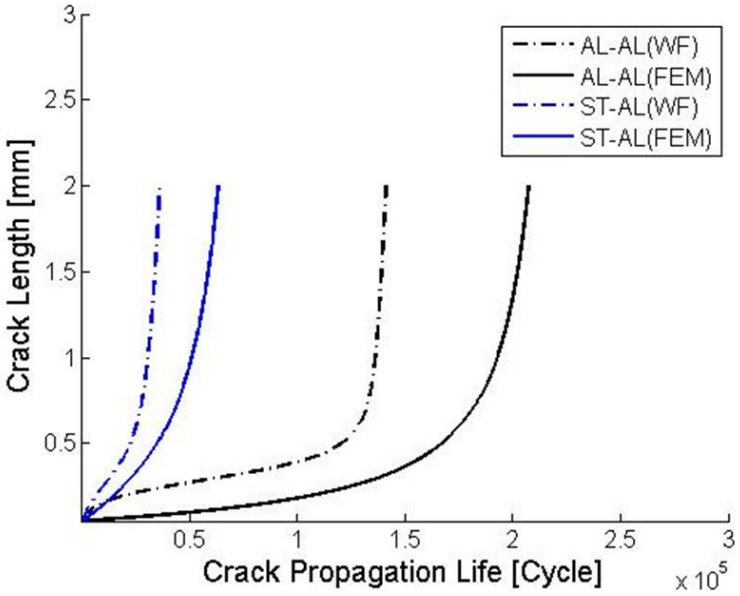


Figure 3.28. Obtained lives during the crack propagation for both the steel-aluminum contact and aluminum-aluminum contact conditions ($\sigma_a = 1.82$)

It is observed that propagation of the crack in the steel-aluminum contact condition is faster than that of the aluminum-aluminum contact condition. The results obtained from the finite element simulations and the weight function method are close to each other. In the steel-aluminum contact case, most of the crack propagation life is spent to reach the crack size 0.5 mm. This size becomes 1 mm for aluminum-aluminum contact conditions. After that point, the crack propagates relatively quickly up until the failure of the specimen for each case.

### 3.4.5. Total Life Results

The total life of the fretting fatigue life of the specimen is calculated with the crack initiation life result obtained from the Fatemi-Socie multiaxial fatigue criteria and the crack propagation life results, calculated via the weight function method and finite element simulations. Crack initiation lives, crack propagation lives, and total fretting fatigue results obtained from both simulations and experiments are shown in Figure 3.29, Figure 3.30, Table 3.2 and Table 3.3, respectively. The life results provided in cycles. Different lives can be obtained under the same conditions in fatigue experiments. According to Table 3.2 different fretting fatigue lives are observed when the same cyclic stress is applied to the specimens. This scatter can be eliminated by performing more experiments.

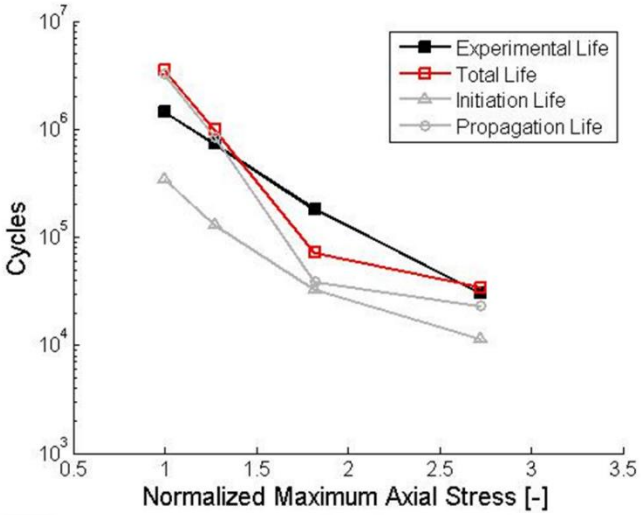


Figure 3.29. Experimental and Numerical fretting fatigue life results for the steel-aluminum contact condition

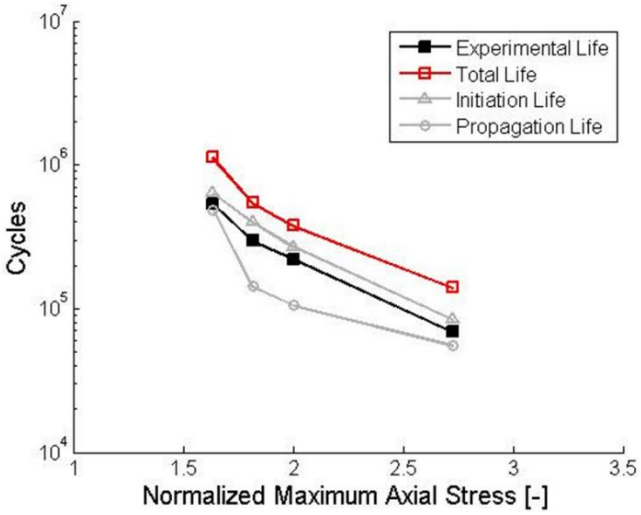


Figure 3.30. Experimental and numerical fretting fatigue life results for the aluminum-aluminum contact condition

Table 3.2. Experimental and simulation results of the steel pad

| Test | $\sigma_a$[-] | $N_i$ | $N_p$ | $N_T$ | $N_{Exp}$ |
|---|---|---|---|---|---|
| 1 | 2.72 | 11,400 | 22,996 | 34,396 | 30,096 |
| 2 | 1.82 | 32,800 | 38,536 | 71,386 | 182,663 |
| 3 | 1.27 | 131,000 | 855,151 | 986,151 | 499,286 |
| 4 | 1.0 | 345,000 | 3,224,061 | 3,569,061 | 1,442,322 |
| 5 | 1.27 | 131,000 | 855,151 | 986,151 | 735,233 |

Table 3.3. Experimental and simulation results of the aluminum pad

| Test | $\sigma_a$[-] | $N_i$ | $N_p$ | $N_T$ | $N_{Exp}$ |
|---|---|---|---|---|---|
| 6 | 1.82 | 400,000 | 142,678 | 542,678 | 295,518 |
| 7 | 1.27 | 1,980,000 | 4,712,646 | 6,692,646 | Run-out |
| 8 | 1.63 | 640,000 | 488,737 | 1,128,737 | 538,580 |
| 9 | 2.72 | 84,000 | 55,579 | 139,579 | 69,143 |
| 10 | 2 | 270,000 | 105,939 | 375,939 | 220,223 |

# CHAPTER 4

# DISCUSSION AND COMPARISON

## 4.1. Discussion

In this part of the study, the stick-slip relations on the contact surface are discussed for the conditions of aluminum-aluminum contact and steel-aluminum contact. Stick and slip regions on the contact surface of the substrate material are given in Figure 4.1. Deformation of the pad and the specimen during the maximum cycle are representatively shown in Figure 4.1a. The stick-slip areas on the total contact area for the specimen are shown in Figure 4.1b (steel pad) and Figure 4.1c (aluminum pad). The applied normalized axial stress is 1.82 in both cases. It is observed that the deformation of the fretting pads affects the contact conditions on the specimen. Aluminum material is less stiff than steel material. Thus, the aluminum pad shows larger deformation when it is compared with the steel pad. Deformation on the pad feet occurs in the direction of the cyclic axial stress. According to Figure 4.1c, deformation on the aluminum pad feet leads to a decrease in the slip area. A relative slip only occurs at the trailing edge of the contact area. For the steel-aluminum contact condition, a relative slip occurs in both the leading and trailing edges of the contact area. Both normalized tangential stress and normalized relative slip values on the specimen surface (aluminum-aluminum contact) under tension and compression loading are shown in Figure 4.2 and Figure 4.3 respectively.

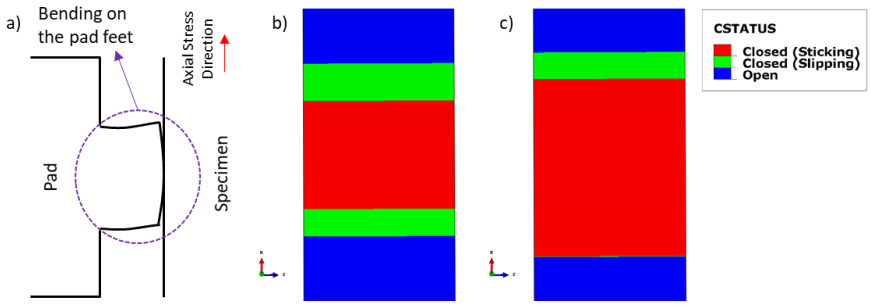


Figure 4.1. (a) Representative bending in the pad feet (b) contact condition on the specimen with the steel pad ($\sigma_a = 1.82$), (c) contact condition on the specimen with the aluminum pad ($\sigma_a = 1.82$)

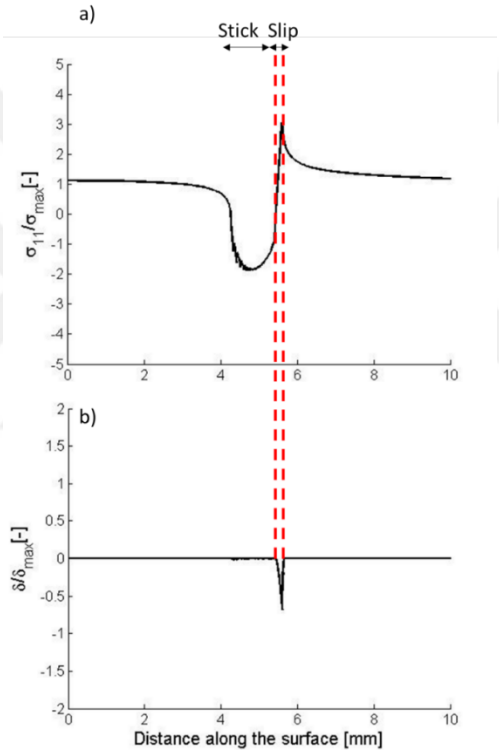


Figure 4.2. (a) Normalized tangential stress distribution, (b) normalized relative slip values on the specimen surface under tension loading ($\sigma_a = 1.82$)

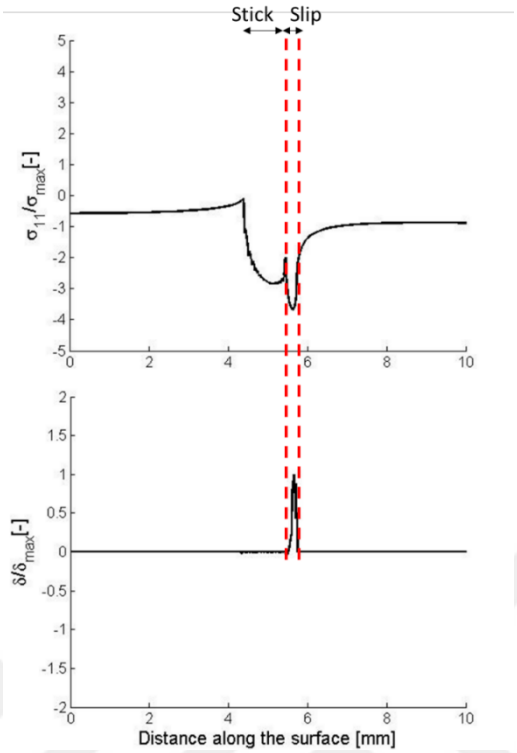


Figure 4.3. (a) Normalized tangential stress distribution, (b) normalized relative slip values on the specimen surface under compression loading ($\sigma_a = 1.82$)

A relation could be attained between the tangential stress distribution and the relative slip behavior on the contact surface according to Figure 39. The slip region is observed closer to the trailing edge under both tension and compression loading. It seems that the location where the maximum tangential stress is observed shows the end of the contact area.

Similar results for the contact conditions are also observed from experiments. The contact surfaces of the failed specimens are shown in Figure 4.4a and Figure 4.4b for the steel-aluminum contact condition and the aluminum-aluminum contact condition, respectively. The other striking result of the analysis is that the location of the stick-slip boundary on the trailing edge is also dependent on the pad material. The stick-slip boundary becomes closer to the end of the contact area when the conditions are aluminum-aluminum contact.

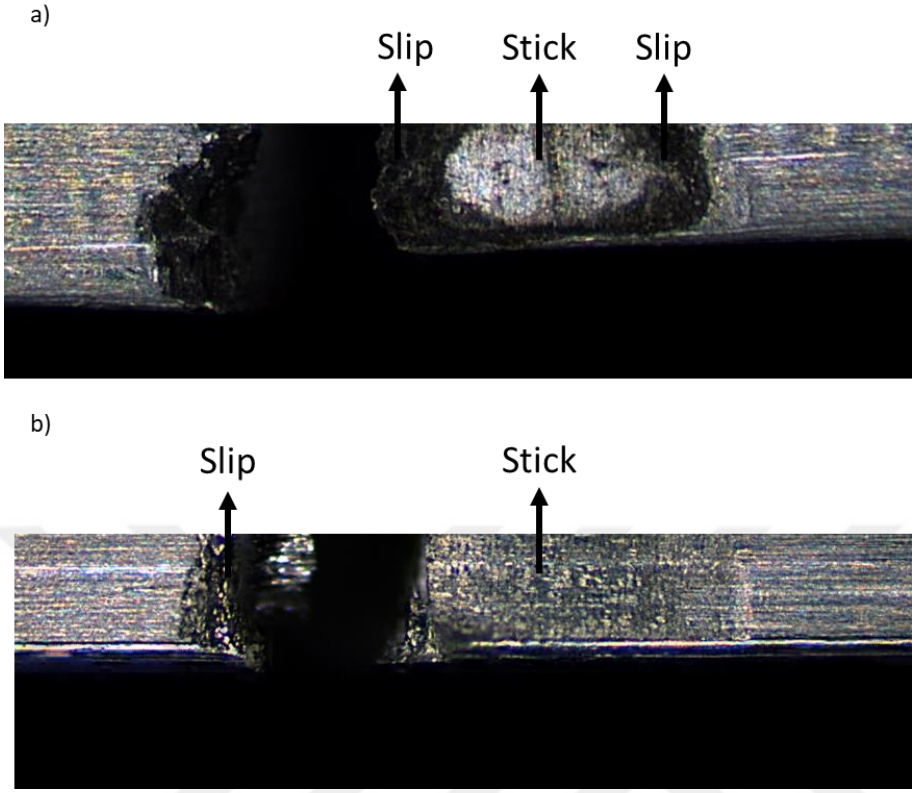


Figure 4.4. Deformation and the contact condition of the failed specimen ($\sigma_a$ =2.72) with (a) steel pad (b) aluminum pad

### 4.2. Comparison

One of the main objectives of this study is to compare the experimental and simulation results obtained from the weight function method and seam crack approach in terms of fretting fatigue lives and fatigue strength reduction factor. Results are obtained from the reduction factors are also used to calculate the error between the results from the simulations and experiments.

#### 4.2.1. Fretting Fatigue Lives

The fretting phenomenon causes a reduction in the material fatigue life. In this section, estimated and observed fretting fatigue lives are compared. In both cases it is observed that the fretting fatigue life of the specimen depends on the pad material stiffness. It was observed that a steel pad lowers the fretting fatigue life in experiments. Although

simulation and experiment results are not exactly the same, they do point in the same direction and experiment results confirm the simulation outputs.

In the low cycle regimes, experimental and simulation results are close to each other. However, in the high cycle regimes, simulation results predict longer lives. The comparison results in terms of fatigue cycles are given in Figure 4.5. The ST pad indicates the comparison of the experiments which were performed with steel pads and the weight function method. The AL pad indicates the comparison of the experiments which were performed with aluminum pads and the weight function method. Simulation results represent the results obtained from seam crack methodology. In the figure, the horizontal axis shows the results obtained from the experiments, and the vertical axis represents the finite element results. The results are given according to logarithmic scale. In this study, the factor of two curves is used to validate the estimated results. These curves are denoted with a dashed line.

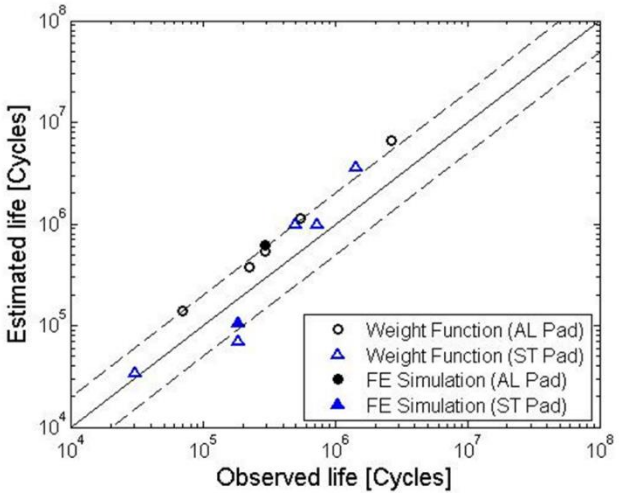


Figure 4.5. Fretting fatigue test results in both experiments and predictions

According to Figure 4.5, the results obtained from the weight function method and from Seam crack methodology are in between a factor of 2 curves.

### 4.2.2. Error Comparison

The aim of the study examined herein has been to understand the effects of dissimilar mating materials on the substrate. To put together all the analyses done in the previous sections, it is necessary to come up with the applied axial cyclic stress- fatigue life relation in both low cycle and high cycle fatigue regimes. Experimental and simulation results are compared in terms of fatigue strength reduction factor, $k_f$, which is defined as the ratio of fatigue strength of the unfretted and fretted materials at the same fatigue life. In engineering designs, these reduction factors are commonly used in optimization procedure in terms of fatigue. The representative maximum stress and life curves are shown in Figure 4.6 to obtain the fatigue strengths of unfretted and fretted specimens for the same number of cycles.

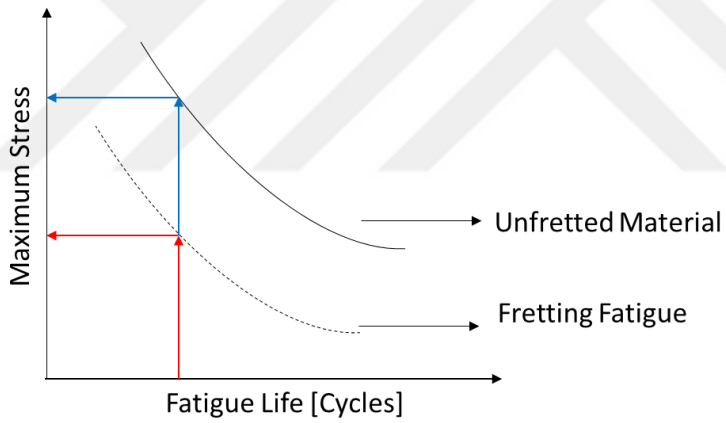


Figure 4.6. Representative SN curve of the unfretted and fretted specimens

Fatigue strength reduction factors are also used in order to calculate the error percentage of the simulations. The error can be calculated as follows,

$$\%Error = \frac{k_{f,experiment} - k_{f,simulation}}{k_{f,experiment}} * 100\ . \tag{4.1}$$

The obtained reduction factors from the experiments, the simulations from the weight function method and the calculated error for each loading case are presented in Table 4.1.

Table 4.1. Experimental and simulation reduction factor results

| Test | $\sigma_a$[-] | $k_f$ [Experiment] | $k_f$ [FEM] | %Error |
|---|---|---|---|---|
| 1 | 2.72 | 1.69 | 1.64 | 2.95 |
| 2 | 1.82 | 1.75 | 2.01 | -18.9 |
| 3 | 1.27 | 2.1 | 1.89 | 10.06 |
| 4 | 1 | 2.27 | 2.02 | 10.96 |
| 5 | 1.27 | 1.97 | 1.89 | 4.34 |
| 6 | 2.72 | 1.42 | 1.23 | 13.17 |
| 7 | 2 | 1.54 | 1.38 | 10.45 |
| 8 | 1.82 | 1.6 | 1.46 | 8.73 |
| 9 | 1.63 | 1.61 | 1.44 | 10.7 |
| 10 | 1.27 | 1.65 | 1.48 | 9.92 |

According to Table 4.1, the fatigue strength reduction factors obtained from both the experiments and simulations are reversely proportional with the axial cyclic loading. Lower reduction factor values are obtained for the steel pad when it is compared with the aluminum pad in both low cycle fatigue and high cycle fatigue regimes. The reduction factor increases in the high cycle fatigue regimes in both of the pad materials, which means the fretting phenomenon is more detrimental for high cycle fatigue regime. It was observed that fatigue limit of AL7050 T7451 material decreases by nearly 60 percent when using steel fretting pads, on the other hand, it decreases by 40 percent with aluminum fretting pad in high cycle fatigue regime.

# CHAPTER 5

## CONCLUSIONS

In this study, the effects of dissimilar mating materials on the fatigue life of the substrate material under fretting fatigue conditions are examined by both performing fretting fatigue experiments using cylindrical-on-flat contact configuration under the same normal load, and making use of finite element simulation analyses. The results of the experiments have been compared in terms of friction force variations with number of cycles, stick and slip in the contact region, and crack propagation behavior. Later, the results of the experiments have been compared to the simulations in terms of fretting fatigue lives and fatigue strength reduction factors. The following conclusions are drawn from this study:

Experimental results show that:

1. The fretting phenomenon is found to be more detrimental (reduction in fatigue life) in high cycle fatigue regimes compared to that experienced in low cycle fatigue regimes. In other words, the fatigue strength reduction factor decreases in the low cycle fatigue regime.
2. The fretting fatigue life is found to depend on the pad material under the same applied normal load condition. It is observed that the fretting fatigue life decreases when the pad material is steel instead of aluminum alloy. This observation is in contrast to the results found in literature which were conducted under the same pressure.
3. The frictional force coefficient is higher for the condition of aluminum-aluminum contact than the steel-aluminum contact.
4. According to the frictional force hysteresis loop results at different cycles, contact condition may change during the experiment. It is observed that in some cases, gross sliding turn into partial slip. This phenomenon is called as bedding in process.

Finite element results show that:

1. The fretting fatigue lives obtained from the finite element simulations are in between the factor of 2 curves when the results are compared with experimental results. Finite element simulations were able to capture the total life time for both cases within an error of 18.9 percent for low cycle fatigue regime and 13 percent for high cycle fatigue regime.
2. The fretting phenomenon is more damaging in the high cycle fatigue regimes when compared to low cycle fatigue regimes. This result also implies that the fatigue strength reduction factor decreases in a low cycle fatigue regime, which is in agreement with the experiments performed.
3. Simulation results show that the fretting fatigue life of a specimen is dependent on the pad material. Using steel pad material instead of aluminum causes the reduction in the fretting fatigue lives of the aluminum alloy under the same normal load conditions.
4. The effect of the pad feet bending on the contact region is observed in terms of stick and slip regions under the same loading conditions. It is observed that the slip region is only formed close to the trailing edge of the contact region for aluminum pads. However, in case of steel pads, slip regions exist at both the leading and trailing edges of the contact area and the stick region is observed to be at the center of the contact region. These findings indicate that fretting scars at the contact region are dependent on the pad material.

While this study is expected to contribute to the existing literature on fretting phenomenon on similar and dissimilar mating materials by incorporating aluminum-aluminum and aluminum–steel interaction and comparisons in the discussion; it also has the potential to inspire and lead to a number of practical solutions in different fields:

For industrial applications, mating materials should be selected as aluminum-aluminum rather than steel-aluminum for the design of the critical parts under cyclic

loading. In addition, the edges of the contacting surfaces should be rounded instead of having sharp edges to avoid singularity at the contact surfaces which leads to plastic deformation on the structure.

From an analysis point of view, a reduction factor should be used in the stress-life curves in the optimization and life estimation analysis of the fatigue critical structures under the chafing condition. If possible, component level testing could increase the reliability of the structures in terms of fatigue life and would allow designers to avoid over design due to high reduction factors.

For those that intend to construct a fretting fatigue test apparatus, the weight of the test setup should be as low as possible to avoid unnecessary inertial forces. During the execution of the test, the pad and proving ring should be instrumented to measure the applied load on the specimen.

As a future work, effect of the plasticity on the contact region will be investigated. Three-dimensional finite element model will be generated and results will be compared with two-dimensional finite element model.

## REFERENCES


[1] Vingsbo, O., & Söderberg, S. (1988). On fretting maps. Wear, 126(2), 131-147. doi: 10.1016/0043-1648(88)90134-2

[2] Eden, E. M., Rose, W. N., & Cunningham, P. L. (1911). The Endurance of Metals: Experiments on Rotating Beams at University College, London. Proceedings of the Institution of Mechanical Engineers,81(1), 839-974. doi:10.1243/pime_proc_1911_081_017_02

[3] Waterhouse, R. B. (1992). Fretting fatigue. International Materials Reviews,37(1), 77-98. doi:10.1179/imr.1992.37.1.77

[4] Lee, B., Suh, J., Lee, H., & Kim, T. (2011). Investigations on fretting fatigue in aircraft engine compressor blade. Engineering Failure Analysis,18(7), 1900 1908. doi:10.1016/j.engfailanal.2011.07.021

[5] Rajasekaran, R., & Nowell, D. (2006). Fretting fatigue in dovetail blade roots:Experiment and analysis. Tribology International, 39(10), 1277 1285. doi:10.1016/j.triboint.2006.02.044

[6] Han, L., Chen, Y. K., Chrysanthou, A., & O'Sullivan, J. M. (2002). Self-Pierce Riveting: A New Way for Joining Structures. Emerging Technologies in Fluids, Structures and Fluid Structure Interactions: Volume 2, Shock, Wave Propagation, Tube Bundle Dynamics, and Structural Dynamics. doi: 10.1115/pvp2002-1495

[7] Collini, L., & Degasperi, F. (2014). MRT detection of fretting fatigue cracks in a cableway locked coil rope. Case Studies in Nondestructive Testing and Evaluation, 2, 64–70. doi: 10.1016/j.csndt.2014.09.001

[8] Nicholas, T. (2006). High cycle fatigue: A mechanics of materials perspective Oxford: Elsevier.

[9] Warlow-Davies, E. J. (1941). Fretting Corrosion and Fatigue Strength: Brief Results of Preliminary Experiments. Proceedings of the Institution of Mechanical Engineers,146(1), 32-38. doi:10.1243/pime_proc_1941_146_012_02

[10] Mall, S., Jain, V., Namjoshi, S., & Lykins, C. (2003). Fretting Fatigue Crack Initiation Behavior of Ti-6Al-4V. Fretting Fatigue: Advances in Basic Understanding and Applications. doi:10.1520/stp10769s

[11] Fellows, L., Nowell, D., & Hills, D. (1997). On the initiation of fretting fatigue cracks. Wear, 205(1-2), 120-129. doi: 10.1016/s0043-1648(96)07302-4

[12] Endo, K., & Goto, H. (1977). Reply to comments on "initiation and propagation of fretting fatigue cracks". Wear, 43(2), 269-270. doi:10.1016/00431648(77)90122-3

[13] Lindley, T. (1997). Fretting fatigue in engineering alloys. International Journal of Fatigue, 19(93), 39-49. doi: 10.1016/s0142-1123(97)00039-x

[14] Adibnazari, S., & Hoeppner, D. W. (1993). A fretting fatigue normal pressure threshold concept. Wear, 160(1), 33-35. doi:10.1016/00431648(93)90403-9

[15] Nakazawa, K., Sumita, M., & Maruyama, N. (1992). Effect of Contact Pressure on Fretting Fatigue of High Strength Steel and Titanium Alloy. Standardization of Fretting Fatigue Test Methods and Equipment. doi:10.1520/stp25824s

[16] Lindley, T., & Nix, K. (2009). Fretting Fatigue in the Power Generation Industry: Experiments, Analysis, and Integrity Assessment. Standardization of Fretting Fatigue Test Methods and Equipment. doi: 10.1520/stp25828s

[17] Spink, G. (1990). Fretting fatigue of a NiCrMoV low pressure turbine shaft steel — the effect of different contact pad materials and of variable slip amplitude. Wear, 136(2), 281-297. doi: 10.1016/0043-1648(90)90152-z

[18] Lee, H., & Mall, S. (2004). Effect of dissimilar mating materials and contact force on fretting fatigue behavior of Ti–6Al–4V. Tribology International, 37(1), 35-44. doi: 10.1016/s0301-679x (03)00112-9

[19] Lykins, C. (2001). Combined experimental–numerical investigation of fretting fatigue crack initiation. International Journal of Fatigue, 23(8), 703-711. doi:10.1016/s0142-1123(01)00029-9

[20] Navarro, C., Garcia, M., & Dominguez, J. (2003). A procedure for estimating the total life in fretting fatigue. Fatigue Fracture of Engineering Materials and Structures, 26(5), 459-468. doi:10.1046/j.1460-2695.2003.00647.x

[21] Lanoue, F., Vadean, A., & Sanschagrin, B. (2009). Finite element analysis and contact modelling considerations of interference fits for fretting fatigue strength calculations. Simulation Modelling Practice and Theory, 17(10), 1587-1602. doi:10.1016/j.simpat.2009.06.017

[22] Wang, D., Zhang, D., Wang, S., & Ge, S. (2013). Finite element analysis of hoisting rope and fretting wear evolution and fatigue life estimation of steel wires. Engineering Failure Analysis, 27, 173-193. doi:10.1016/j.engfailanal.2012.08.014

[23] Mcveigh, P. A., & Farris, T. N. (1997). Finite Element Analysis of Fretting Stresses. Journal of Tribology, 119(4), 797. doi:10.1115/1.2833887

[24] Madge, J., Leen, S., & Shipway, P. (2008). A combined wear and crack nucleation–propagation methodology for fretting fatigue prediction. International Journal of Fatigue, 30(9), 1509–1528. doi: 10.1016/j.ijfatigue.2008.01.002

[25] Araújo, J. A., Nowell, D., & Vivacqua, R. C. (2004). The use of multiaxial fatigue models to predict fretting fatigue life of components subjected to different contact stress fields. Fatigue & Fracture of Engineering Materials & Structures, 27(10), 967-978. doi:10.1111/j.1460-2695.2004.00820.x

[26] Lee, Y.-L., Barkey, M. E., & Kang, H.-T. (2012). Metal fatigue analysis handbook: practical problem-solving techniques for computer-aided engineering. Waltham, MA: Butterworth-Heinemann.

[27] Sum, W., Williams, E., & Leen, S. (2005). Finite element, critical-plane, fatigue life prediction of simple and complex contact configurations. International Journal of Fatigue, 27(4), 403-416. doi:10.1016/j.ijfatigue.2004.08.001

[28] Neu, R., Pape, J., & Swalla, D. (2000). Methodologies for Linking Nucleation and Propagation Approaches for Predicting Life under Fretting Fatigue. Fretting Fatigue: Current Technology and Practices. doi: 10.1520/stp14742s

[29] Giannakopoulos, A., Lindley, T., & Suresh, S. (1998). Aspects of equivalence between contact mechanics and fracture mechanics: Theoretical connections and a life-prediction methodology for fretting-fatigue. Acta Materialia, 46(9), 2955 2968. doi:10.1016/s1359-6454(98)00011-1

[30] Golden, P., & Grandt, A. (2004). Fracture mechanics based fretting fatigue life predictions in Ti–6Al–4V. Engineering Fracture Mechanics, 71(15), 2229-2243. doi:10.1016/j.engfracmech.2003.10.005

[31] Giannakopoulos, A., Lindley, T., & Suresh, S. (2000). Applications of Fracture Mechanics in Fretting Fatigue Life Assessment. Fretting Fatigue: Current Technology and Practices. doi:10.1520/stp14723s

[32] Nicholas, T. (2003). A fracture mechanics methodology assessment for fretting fatigue. International Journal of Fatigue, 25(9-11), 1069-1077. doi:10.1016/s0142-1123(03)00115-4

[33] Navarro, C., Muñoz, S., & Domínguez, J. (2006). Propagation in fretting fatigue from a surface defect. Tribology International, 39(10), 1149-1157. doi:10.1016/j.triboint.2006.02.004

[34] Hutson, A., Nicholas, T., & John, R. (2005). Fretting fatigue crack analysis in Ti–6Al–4V. International Journal of Fatigue, 27(10-12), 1582-1589. doi:10.1016/j.ijfatigue.2005.07.008

[35] Hojjati-Talemi, R., Wahab, M. A., Pauw, J. D., & Baets, P. D. (2014). Prediction of fretting fatigue crack initiation and propagation lifetime for cylindrical contact configuration. Tribology International, 76, 73-91. doi:10.1016/j.triboint.2014.02.017

[36] Pereira, K., & Wahab, M. A. (2017). Fretting fatigue crack propagation lifetime prediction in cylindrical contact using an extended MTS criterion for nonproportional loading. Tribology International, 115, 525-534. doi:10.1016/j.triboint.2017.06.026

[37] Giner, E., Navarro, C., Sabsabi, M., Tur, M., Domínguez, J., & Fuenmayor, F. (2011). Fretting fatigue life prediction using the extended finite element method. International Journal of Mechanical Sciences, 53(3), 217-225. doi:10.1016/j.ijmecsci.2011.01.002

[38] Baietto, M., Pierres, E., Gravouil, A., Berthel, B., Fouvry, S., & Trolle, B. (2013). Fretting fatigue crack growth simulation based on a combined experimental and XFEM strategy. International Journal of Fatigue, 47, 31-43. doi:10.1016/j.ijfatigue.2012.07.007

[39] Giner, E., Tur, M., Vercher, A., & Fuenmayor, F. (2009). Numerical modelling of crack–contact interaction in 2D incomplete fretting contacts using X FEM. Tribology International,42(9), 1269-1275. doi:10.1016/j.triboint.2009.04.003

[40] Pauw, J. D., Baets, P. D., Waele, W. D., & Hojjati-Talemi, R. (2014). Design of a fretting fatigue test rig with compliant springs. International Journal Sustainable Construction & Design, 4(2). doi: 10.21825/scad.v4i2.1074

[41] Wittkowsky, Birch, Dominguez, & Suresh. (1999). An apparatus for quantitative fretting testing. Fatigue & Fracture of Engineering Materials & Structures, 22(4), 307–320. doi: 10.1046/j.1460-2695.1999.00145.x

[42] Zalnezhad, E., Sarhan, A. A. D., & Jahanshahi, P. (2013). A new fretting fatigue testing machine design, utilizing rotating–bending principle approach. The International Journal of Advanced Manufacturing Technology, 70(9-12), 2211 2219. doi: 10.1007/s00170-013-5457-0

[43] Swalla, D., & Neu, R. (2001). Influence of coefficient of friction on fretting fatigue crack nucleation prediction. Tribology International, 34(7), 493-503. doi: 10.1016/s0301-679x (01)00048-2

[44] Mcveigh, P. (1999). Modeling interfacial conditions in nominally flat contacts for application to fretting fatigue of turbine engine components. International Journalof Fatigue, 21, 157-165. doi:10.1016/s0142-1123(99)00067-5

[45] Hutson, A., & Nicholas, T. (n.d.). Fretting Fatigue Behavior of Ti-6Al-4V against Ti-6Al-4V under Flat-on-Flat Contact with Blending Radii. Fretting Fatigue: Current Technology and Practices. doi: 10.1520/stp14738s

[46] Martins, L. H. L., Rossino, L. S., Filho, W. W. B., & Araújo, J. A. (2008). Detailed design of fretting fatigue apparatus and tests on 7050-T7451 Al alloy. Tribology - Materials, Surfaces & Interfaces, 2(1), 39–49. doi:10.1179/175158308x320764

[47] Arora, P., Jacob, M., Salit, M., Ahmed, E., Saleem, M., & Edi, P. (2007). Experimental evaluation of fretting fatigue test apparatus. International Journal of Fatigue, 29(5), 941–952. doi: 10.1016/j.ijfatigue.2006.07.012

[48] Mugadu, A., Hills, D., & Nowell, D. (2002). Modifications to a fretting-fatigue testing apparatus based upon an analysis of contact stresses at complete and nearly complete contacts. Wear, 252(5-6), 475–483. doi:10.1016/s00431648(02)00007-8

[49] Mccarthy, O., Mcgarry, J., & Leen, S. (2013). Microstructure-sensitive prediction and experimental validation of fretting fatigue. Wear, 305(1-2), 100–114. doi:10.1016/j.wear.2013.05.012

[50] Majzoobi, G., Hojjati, R., & Soori, M. (2011). Fretting fatigue behavior of Al7075-T6 at sub-zero temperature. Tribology International, 44(11), 1443–1451. doi: 10.1016/j.triboint.2011.03.021

[51] Attia, M. H. (1992). Standardization of fretting fatigue test methods and equipment. Philadelphia, PA: ASTM.

[52] Pape, J., & Neu, R. (1999). Influence of contact configuration in fretting fatigue testing. Wear, 225-229, 1205-1214. doi: 10.1016/s0043-1648(98)00398-6

[53] Neu, R. (2011). Progress in standardization of fretting fatigue terminology and testing. Tribology International, 44(11), 1371-1377.

[54] Wallace, J. M., & Neu, R. W. (2003). Fretting fatigue crack nucleation in Ti-6Al 4V. Fatigue Fracture of Engineering Materials and Structures, 26(3), 199-214. doi:10.1046/j.1460-2695.2003.00553.x

[55] MMPDS-07: Metallic materials properties development and standardization (MMPDS). (2012). Washington, D.C.: Federal Aviation Administration.

[56] NASGRO. Fracture mechanics and fatigue crack growth analysis software (2006). v5.0, NASA-JSC and Southwest Research Institute.

[57] Rossino, L., Castro, F., Filho, W. B., & Araújo, J. (2009). Issues on the mean stress effect in fretting fatigue of a 7050-T7451 Al alloy posed by new experimental data. International Journal of Fatigue,31(11-12), 2041-2048. doi:10.1016/j.ijfatigue.2008.12.011

[58] Szolwinski, M. P., & Farris, T. N. (1998). Observation, analysis and prediction of fretting fatigue in 2024-T351 aluminum alloy. Wear, 221(1), 24-36. doi:10.1016/s0043-1648(98)00264-6

[59] Rayaprolu, D., & Cook, R. (2009). A Critical Review of Fretting Fatigue Investigations at the Royal Aerospace Establishment. Standardization of Fretting Fatigue Test Methods and Equipment. doi:10.1520/stp25826s

[60] Goh, C., Wallace, J., Neu, R., & Mcdowell, D. (2001). Polycrystal plasticity simulations of fretting fatigue. International Journal of Fatigue, 23, 423-435. doi:10.1016/s0142-1123(01)00150-5

[61] Hertz, H. (1881). On the contact of elastic solids. J. reine angew. Math, 92, 156 171. doi: 10.1515/crll.1882.92.156

[62] Mindlin, R. D., & Deresiewicz, H. (1989). Elastic Spheres in Contact Under Varying Oblique Forces. The Collected Papers of Raymond D. Mindlin Volume I, 269–286. doi: 10.1007/978-1-4613-8865-4_35

[63] Fatemi, A., & Socie, D. F. (1988). A Critical Plane Approach to Multiaxial Fatigue Damage Including Out-Of-Phase Loading. Fatigue & Fracture of Engineering Materials and Structures,11(3), 149-165. doi:10.1111/j.14602695.1988.tb01169.x

[64] Li, X., Zuo, Z., & Qin, W. (2015). A fretting related damage parameter for fretting fatigue life prediction. International Journal of Fatigue,73, 110-118. doi:10.1016/j.ijfatigue.2014.12.003

[65] Araújo, J. (2002). The effect of rapidly varying contact stress fields on fretting fatigue. International Journal of Fatigue,24(7), 763-775. doi:10.1016/s01421123(01)00191-8

[66] Giner, E., Sukumar, N., Denia, F., & Fuenmayor, F. (2008). Extended finite element method for fretting fatigue crack propagation. International Journal of Solids and Structures, 45(22-23), 5675-5687. doi:10.1016/j.ijsolstr.2008.06.009

[67] Majzoobi, G., & Abbasi, F. (2017). On the effect of shot-peening on fretting fatigue of Al7075-T6 under cyclic normal contact loading. Surface and Coatings Technology, 328, 292-303. doi:10.1016/j.surfcoat.2017.08.067

[68] Navarro, C., Munoz, S., & Dominguez, J. (2008). On the use of multiaxial fatigue criteria for fretting fatigue life assessment. International Journal of Fatigue, 30(1), 32-44. doi:10.1016/j.ijfatigue.2007.02.018

[69] Antunes, M. A., Silva, C. R. M. D., Rêgo, E. M. F. D., & Miranda, A. C. D. O. (2017). Stress intensity factor solutions for fretting fatigue using stress gradient factor. Engineering Fracture Mechanics, 186, 331–346. doi:10.1016/j.engfracmech.2017.10.031

[70] Chattopadhyay, A., Glinka, G., El-Zein, M., Qian, J., & Formas, R. (2011). Stress Analysis and Fatigue of welded structures. Welding in the World,55(7-8), 2-21. doi:10.1007/bf03321303

[71] ABAQUS/Standard: User's manual. (2007). Providence, RI: Hibbitt, Karlsson & Sorensen.

[72] Nikishkov, G. P. (2013). Accuracy of Quarter-point Element in Modeling Crack tip Fields. Computer Modeling in Engineering and Sciences, 93(5), 335–361.

[73] Erdogan, F., & Sih, G. C. (1963). On the Crack Extension in Plates Under Plane Loading and Transverse Shear. Journal of Basic Engineering,85(4), 519. doi:10.1115/1.3656897

[74] Korkmaz, Y. M., & Coker, D. (2017). Finite element analysis of fretting contact for dissimilar and nonhomogeneous materials. Procedia Structural Integrity,5, 452-459. doi:10.1016/j.prostr.2017.07.196

[75] Zhang, T., Mchugh, P., & Leen, S. (2012). Finite element implementation of multiaxial continuum damage mechanics for plain and fretting fatigue. International Journal of Fatigue, 44, 260–272. doi:10.1016/j.ijfatigue.2012.04.011

[76] Lykins, C. D., Mall, S., & Jain, V. (2001). A shear stress-based parameter for fretting fatigue crack initiation. Fatigue Fracture of Engineering Materials and Structures, 24(7), 461–473. doi: 10.1046/j.1460-2695.2001. 00412.x

[77] Korkmaz, Y. M., & Coker, D. (2018). Finite element analysis of fretting contact for nonhomogenous materials. IOP Conference Series: Materials Science and Engineering,295, 012006. doi:10.1088/1757-899x/295/1/012006

[78] Hojjati-Talemi, R., Wahab, M. A., & Baets, P. D. (2012). Numerical Investigation into the Effect of Contact Geometry on Fretting Fatigue Crack Propagation Lifetime. Tribology Transactions, 55(3), 365-375. doi:10.1080/10402004.2012.658987

# APPENDICES

## A. Dimensions of the Fretting Fatigue Test Apparatus

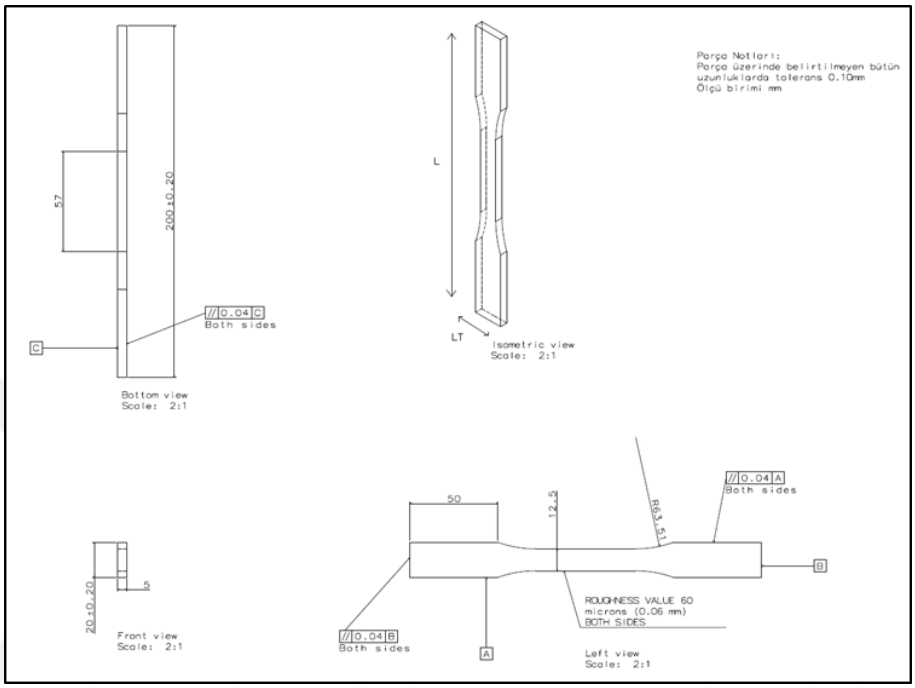


Figure 0.1. CAD drawing of the specimen

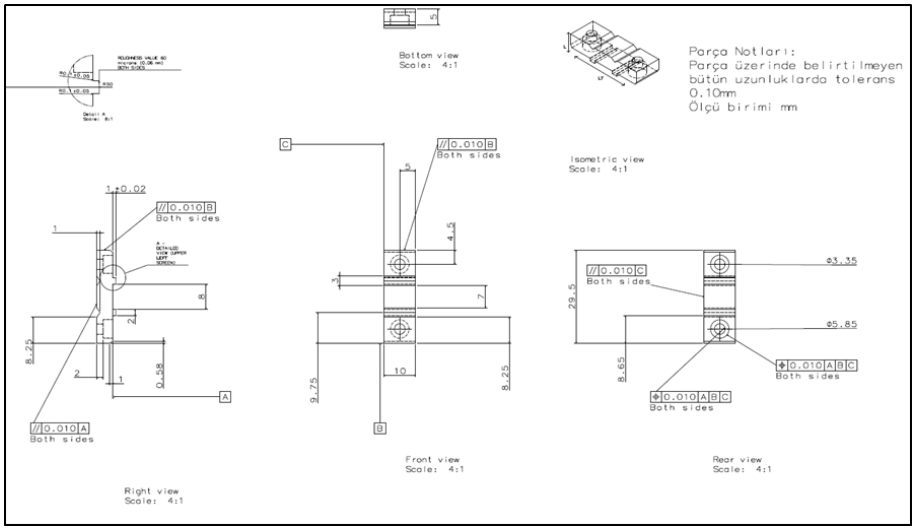


Figure 0.2. CAD drawing of the fretting pad

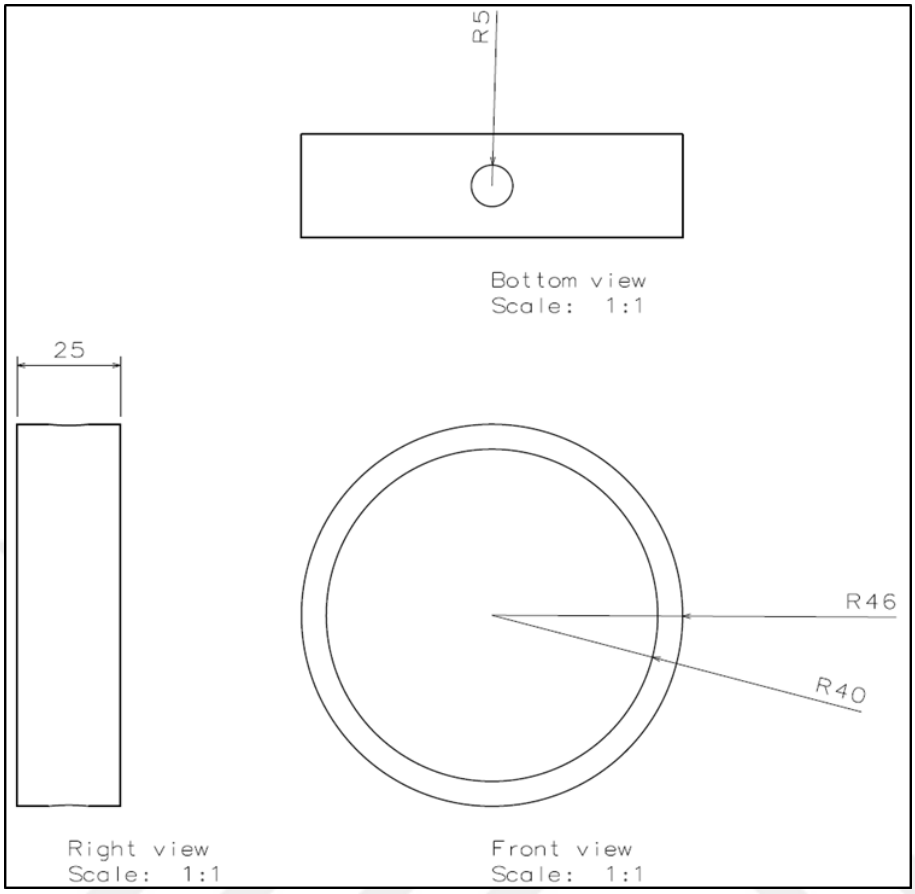


Figure 0.3. CAD drawing of the proving ring

## B. **Friction Variation Curves**

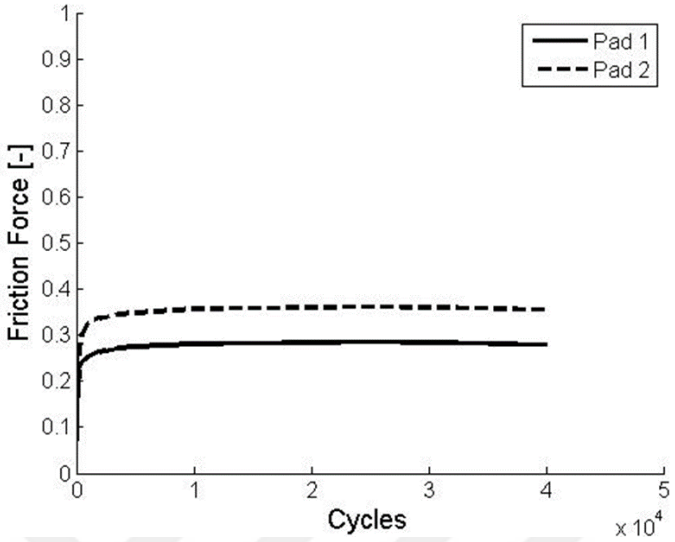


Figure 0.4. Friction variation curve of the test 2

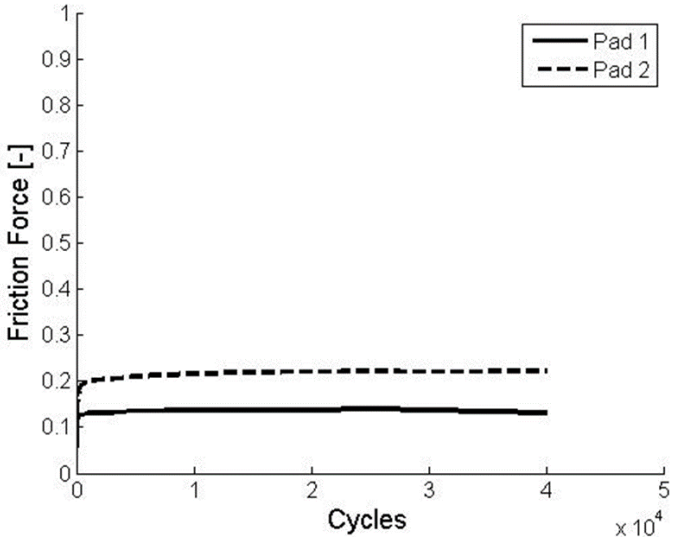


Figure 0.5. Friction variation curve of the test 3

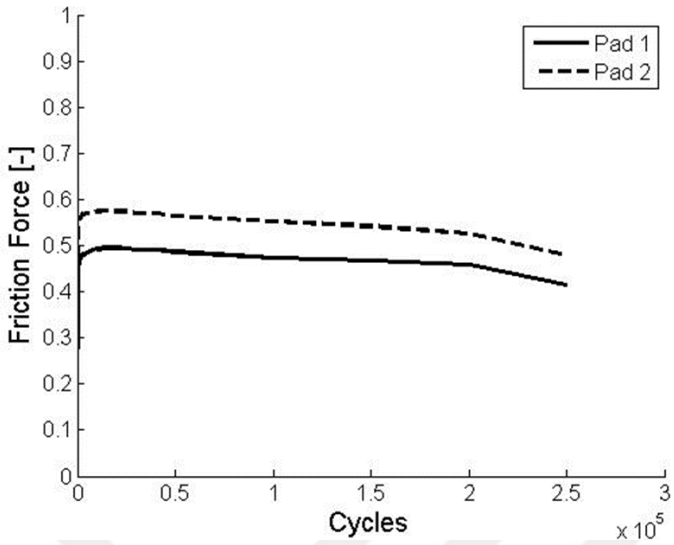


Figure 0.6. Friction variation curve of the test 6

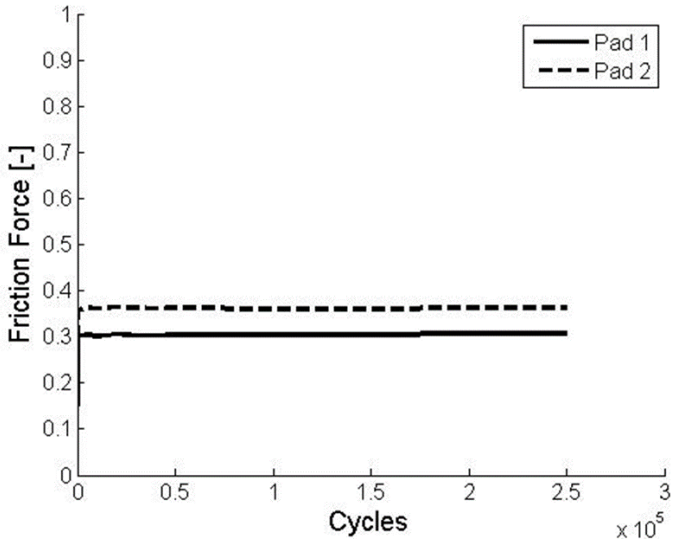


Figure 0.7. Friction variation curve of the test 7

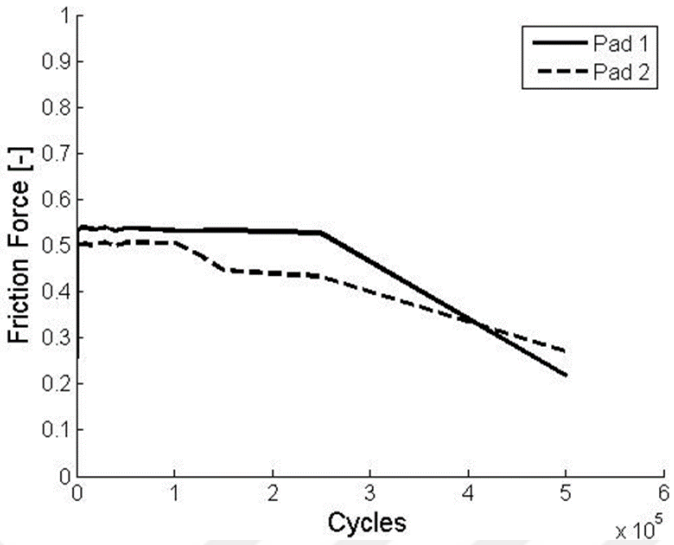


Figure 0.8. Friction variation curve of the test 8

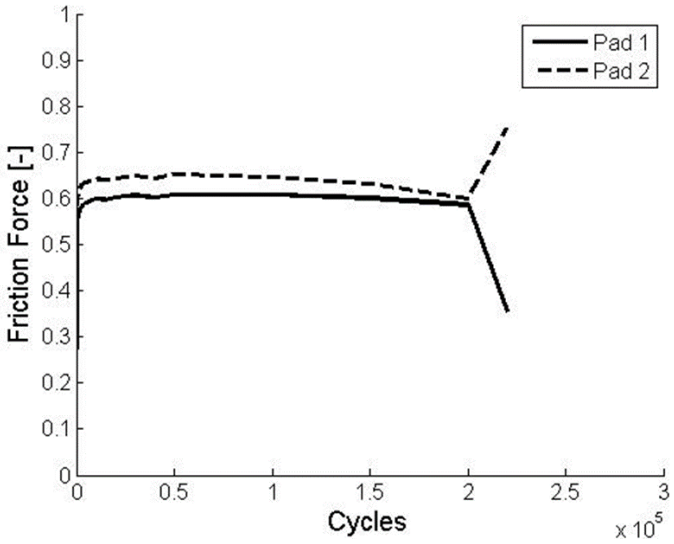


Figure 0.9. Friction variation curve of the test 10

## C. Crack Initiation Life Calculation MATLAB Code

```
clear all;clc;
%close all;format long
hold on

teta=-90/180*pi:10/180*pi:90/180*pi;
%
k=input;
Sigmayield=input;
S11_Max=xlsread('MAX_CYCLE_S11.xlsx');
S22_Max=xlsread('MAX_CYCLE_S22.xlsx');
S21_Max=xlsread('MAX_CYCLE_S12.xlsx');
E11_Max=xlsread('MAX_CYCLE_E11.xlsx');
E22_Max=xlsread('MAX_CYCLE_E22.xlsx');
E21_Max=xlsread('MAX_CYCLE_E12.xlsx');

S11_Min=xlsread('MIN_CYCLE_S11.xlsx');
S22_Min=xlsread('MIN_CYCLE_S22.xlsx');
S21_Min=xlsread('MIN_CYCLE_S12.xlsx');
E11_Min=xlsread('MIN_CYCLE_E11.xlsx');
E22_Min=xlsread('MIN_CYCLE_E22.xlsx');
E21_Min=xlsread('MIN_CYCLE_E12.xlsx');

for j=1:length(teta)
    for i=1:length(S11_Max)
        Sigman_max(i,1,j)=S11_Max(i,1);
        Sigman_max(i,2,j)       =       (S11_Max(i,2)+S22_Max(i,2))/2+((S11_Max(i,2)-
S22_Max(i,2))/2)*cos(2*teta(j))-S21_Max(i,2)sin(2*teta(j))
        Gama_max(i,1,j)=-((E22_Max(i,2)-E11_Max(i,2))sin(teta(j))/2)*sin(2*teta(j))-
(E21_Mx(i,2)/2)*cos(2*teta(j))

    end
end


for j=1:length(teta)
    for i=1:length(S11_Min)
        Sigman_min(i,1,j)=S11_Min(i,1);
        Sigman_min(i,2,j)       =       (S11_Min(i,2)+S22_Min(i,2))/2+((S11_Min(i,2)-
S22_Mn(i,2))/2)*cos(2*teta(j))-S21_Min(i,2)*sin(2*teta(j));
        Gama_min(i,1,j)=-((E22_Min(i,2)-E11_Min(i,2))*sin(teta(j))/2)*sin(2teta(j))-
(E21_Min(i,2)/2)*cos(2*teta(j));
    end
end

DeltaGamaMax=abs(Gama_max-Gama_min);
for i=1:length(Delta)
[ButunNokDeltaGamaMax(i),Hangi (i)]=max(DeltaMax(i,1,:));
end
for i=1:length(HangiAci)
Sigman_max_MaximCycle(i,1)=Sigman_max(i,2,HangiAci(i));
end
Sigman_max_MaximumCycle=Sigman_max_MaximumCycle';
FS= ButunNoktalarDeltaGamaMax/2.*(1+k*Sigman_max_MaximumCycle/Sigmayield);

plot(Sigman_max(:,1,1),FS,'linewidth',2)
```

## D. Crack Propagation Life Calculation MATLAB and FORTRAN Codes

```
clear all
clc

format long

syms a y F t

a=5.6;
F=1;
t=6.25;

 %Single edge crack in finite plate (M1, M2 and M3)

m1_u=(-0.029207+(a/t)*(0.213074+(a/t)*(-3.029553+(a/t)*(5.901933-(a/t)*2.657820))));
m1_a=(1.0+(a/t)*(-1.259723+(a/t)*(-0.048475+(a/t)*(0.481250+(a/t)*(-
0.526796+(a/t)*(0.345012))))));
m1=m1_u/m1_a;

m2_u=(0.451116+(a/t)*(3.462425+(a/t)*(-1.078459+(a/t)*(3.558573-(a/t)*7.553533))));
m2_a=(1.0+(a/t)*(-1.496612+(a/t)*(0.764586+(a/t)*(-
0.659316+(a/t)*(0.258506+(a/t)*0.114568)))));
m2=m2_u/m2_a;

m3_u=(0.427195+(a/t)*(-3.730114+(a/t)*(16.276333+(a/t)*(-
18.799956+(a/t)*(14.112118)))));
m3_a=(1.0+(a/t)*(-1.129189+(a/t)*(0.033758+(a/t)*(0.192114+(a/t)*(-
0.658242+(a/t)*(0.554666))))));
m3=m3_u/m3_a;

 %Weight function solution

m=((2.0*F)/(sqrt(2*pi*(a-y))))*(1+m1*((1-(y/a))^(0.5))+m2*(1-(y/a))+m3*((1-
(y/a))^(3/2)));

%Sigma calculation

S11=-12*y^6+80*y^5-240*y^4+18*y^3+25*y^2-10*y+35;

w=S11*m;

SIF=vpa(int(w,y,0,a))
```

```
program
real a1,dK_eq,da_dN1,C,n,R,f,p,q,a_zero,Dkth,Dkth2,Kmax,Kc
integer i
C=1.53e-10!Paris law constant
n=2.5!Paris law constant
!$$$$$$ f=0.24375634
f=input
R=input
p=input
q=input
Kc=input
i=1
open(999,file='crack_length.txt',status='replace')
a1=0.05
do while (a1<5.6)
dK_eq=8.87*a1**6-131.08*a1**5+749.6*a1**4-2059.2*a1**3+2822*a1**2-1701*a1+372.82
da_dN1=C*((((1-f)/(1-R))*(dK_eq))**n)
a2=a1+da_dN1
a1=a2
i=i+1
 write(999,*) dK_eq,da_dN1,a2
end do
end program
```

## E. Stress Intensity Factor Calculation for the Single Edge Crack in a Finite Plate

Number of ten contours are taken into account in order to calculate the stress intensity factor. Average stress intensity value computed with using the rest of 8 contours. Von mises stress results can be seen in the figure.

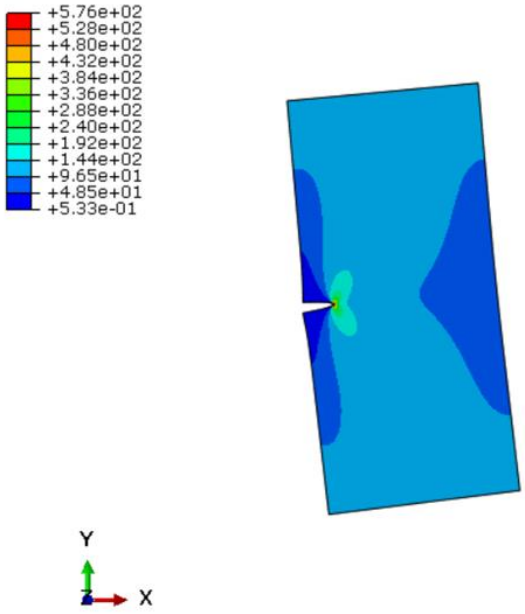


Figure 0.10. Stress contour results of the cracked plate

In order to validate the seam crack methodology capability in terms of stress intensity factor in ABAQUS, SIF values were calculated for the same geometry and the same crack size with using weight function method and NASGRO software. The results are tabulated in the table.

Table 0.1. Stress intensity factor results of the cracked plate

| | ABAQUS | NASGRO | WF METHOD |
|---|---|---|---|
| SIF $[MPa\sqrt{mm}]$ | 211 | 211.93 | 214.4 |

## F. Mesh Sensitivity Study for Cracked Plate

Mesh sensitivity study is performed for the cracked plate to identify the effect of the mesh size on the crack in terms of stress intensity factor. A single edge crack on a finite plate model is considered. Finite element model is constructed in ABAQUS. The dimensions, load and boundary conditions of the model is given in below figure.

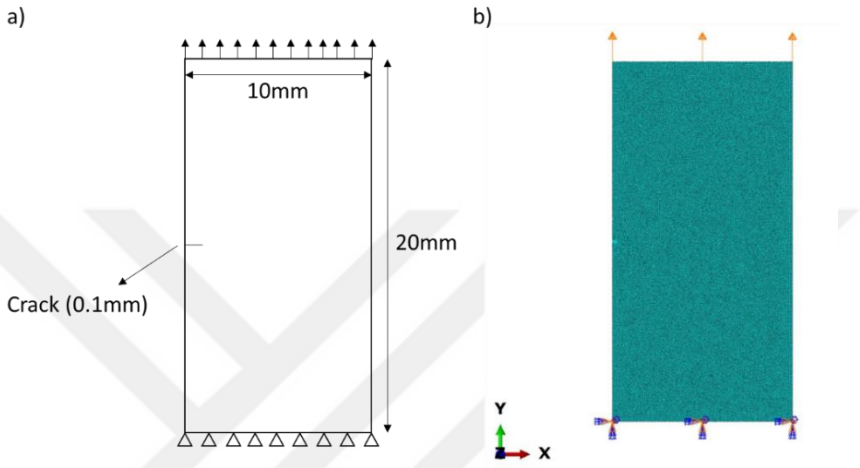


Figure 0.11. (a) Dimensions, loading and boundary conditions, (b) mesh of the finite plate

Seam crack methodology is used to define the crack. The mesh size around the crack region is changed from 0.05 to 0.01 mm. The mesh size around the crack tip is the same in each model. The mesh sizes around the crack for different FE models are shown in figure.

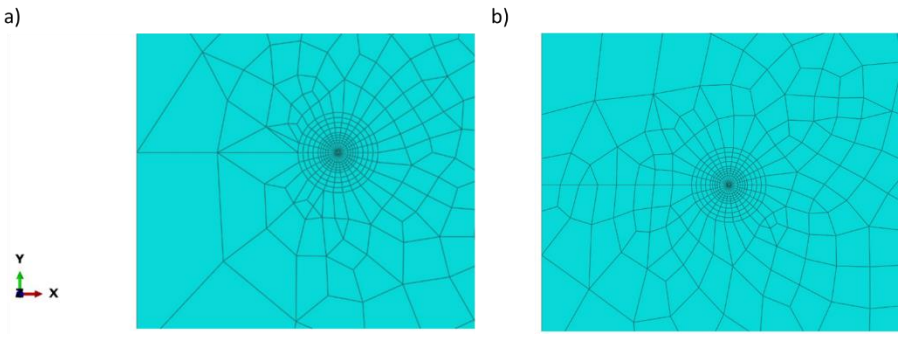


Figure 0.12. Mesh size (a) 0.05 mm, (b) 0.01 mm around the crack faces

The stress intensity factor results are given in below table.

Table 0.2. Stress intensity factor results

| Mesh Size | 0.05 $mm$ | 0.025 $mm$ | 0.01 $mm$ |
|---|---|---|---|
| SIF [$MPa\sqrt{mm}$] | 255,8 | 254,3 | 253,3 |

According to results, stress intensity factor is mostly dependent on the mesh size around the crack tip instead of the mesh size around the crack. Similar stress intensity values are found form the finite element model.